Lightweight and Explainable Deep Learning Model for EV Battery Voltage Prediction

by

Saleh Mohammed Shahriar
B.Sc., Rajshahi University of Engineering & Technology, 2020
A Thesis Submitted in Partial Fulfillment of the
Requirements for the Degree of

MASTER OF APPLIED SCIENCE

in the Department of Electrical & Computer Engineering

Lightweight and Explainable Deep Learning Model for EV Battery Voltage Prediction

by

Saleh Mohammed Shahriar
B.Sc., Rajshahi University of Engineering & Technology, 2020

Supervisory Committee

Dr. Daler N. Rakhmatov, Supervisor
(Department of Electrical & Computer Engineering)

Dr. T. Ilamparithi, Departmental Member
(Department of Electrical & Computer Engineering)

ABSTRACT

Electric vehicles (EVs) play an important role in reducing the greenhouse gas emissions by providing an environment-friendly alternative to the fossil-fuel-based means of transportation. EVs are typically powered by Li-ion battery packs supported by a Battery Management System (BMS). The latter is tasked with monitoring and keeping the battery voltage, current, and temperature within safe operating limits, as well as estimating and improving the battery performance-related parameters, such as the battery state-of-charge and lifespan. In this thesis, we aim to extend the BMS capabilities by enabling battery voltage predictions under a given load profile (i.e., discharge/charge current varying over time). Such predictions are useful for proactive (as opposed to reactive) load management, as they allow a BMS to forecast the battery voltage behaviour under various anticipated load conditions.

Using a data-driven deep learning (DL) approach, we propose a novel model that generates battery voltage estimates given the battery current, temperature, and consumed charge over time. It has a V-shaped architecture that features two wings to enhance the model explainability. The first wing predicts the steady-state open-circuit voltage (OCV) component, based on the consumed battery charge information, while the second wing predicts the transient voltage component, based on the battery current and temperature information. The total number of the model parameters is under 2.6K.

A well-known experimental dataset was used in this study for training, validation, and testing purposes. This dataset contains measurements taken on a Li-ion battery subjected to various EV driving cycles interleaved with charging cycles. The mean absolute percentage error (between predicted and measured battery voltage values) was under 1%, demonstrating the accuracy of the proposed model. Given that a battery must operate within certain maximum and minimum voltage limits, early and accurate voltage estimation has the potential to extend the battery lifetime by enabling proactive optimizations of the battery discharge-charge cycles. An extended battery life implies that a battery-powered EV can remain operational for a longer duration of time, which in turn can facilitate a wider adoption of EVs as an environmentally-friendly transportation alternative.

Contents

List of Tables

List of Figures

List of Acronyms

Adam	Adaptive Moment Estimation
ANN	Artificial Neural Network
BMS	Battery Management System
CARB	California Air Resources Board
CNN	Convolutional Neural Network
DL	Deep Learning
DNN	Deep Neural Network
EPA	Environmental Protection Agency
EV	Electric Vehicle
GPU	Graphics Processing Unit
GRU	Gated Recurrent Unit
LSTM	Long Short Term Memory
MAE	Mean Absolute Error
MAPE	Mean Absolute Percentage Error
MLP	Multilayer Perceptron
OCP	Overcharge Penalty
OCV	Open Circuit Voltage
ODP	Overdischarge Penalty
ReLU	Rectified Linear Unit
RMSPE	Root Mean Square Percentage Error
RNN	Recurrent Neural Network
SHAP	SHapley Additive exPlanations
SoC	State of Charge
SoE	State of Energy
SoH	State of Health

ACKNOWLEDGEMENTS

I would like to thank:

Dr. Daler N. Rakhmatov, for selecting me for his research group and allowing me to research under his wonderful supervision. He has supported me in every difficult situation and encouraged me throughout my master's journey. I have learned from him how a research approach should be and how to think and work to make something creative. I have felt more passionate about my research after joining his research group. It is not possible to express his endeavour in a few lines. I am grateful to him for the motivation I have found in my life.

My Parents, for their unwavering support and sacrifices for me from childhood to this day. They have endured countless hardships throughout their lives, all to see me succeed and fulfill my dreams. Their love, resilience, and dedication have been my greatest source of strength, and I owe every achievement to their selfless support.

My lovely wife, Abida Sultana, for her love and support throughout my life and study. She always inspired me in every hard situation of my life. She is not only my wife but also my best friend.

And my success is only through Allah. Upon Him I have relied, and to Him I return.
The Quran(11:88)

DEDICATION

To my younger sister, Jannatul Ferdous Fatema

Chapter 1

Introduction

1.1 Battery Management Systems

Electric vehicles (EVs) are an important alternative to fossil-fuel-based vehicles that produce carbon dioxide. EVs are environment-friendly and play a significant role in mitigating the issue of global warming [1]. For example, the European Environmental Agency estimated that approximately 800 million tons of EU's greenhouse gas emissions in 2022 were due to the transportation sector, and more than 70% of that amount was attributable to road transport [2]. Hence, putting more EVs on the roads to replace fossil-fuel-based vehicles will have a clear positive impact. Energy storage systems based on Li-ion batteries play a vital role in powering EVs and portable systems [3] due to their high power density and efficiency [4]. A so-called battery management system (BMS) is a crucial component of battery-powered vehicles and devices that enforces a safe and efficient operation of the lithium-ion battery packs [5]. The BMS is designed to perform the following typical tasks [6]:

- Monitoring and communicating the battery temperature, current, and voltage information;
- Protecting the battery pack against excessive current and temperature values;
- Maintaining the battery voltage within the safe operating limits;
- Balancing the charge and discharge currents of individual cells to reduce the cell-to-cell operational mismatch, thus improving the battery pack lifespan;

- Estimating and communicating the battery state-of-charge (SoC), state-of-health (SoH), remaining capacity, and other performance-related characteristics.[1]

In this thesis, we aim to extend the BMS capabilities by enabling the battery voltage predictions under a given load profile (i.e., discharge/charge current varying over time). Such predictions are useful for proactive (as opposed to reactive) load management, as they allow the BMS to forecast the battery voltage behavior under various anticipated load conditions.

1.2 Voltage Prediction

A lithium-ion battery can deliver charge until it reaches its cutoff voltage [7]. However, the discharge rate and temperature determine how much charge can be extracted from the battery before its cutoff voltage is crossed. For instance, at higher discharge rates and lower temperatures, the amount of delivered charge is reduced [8]. If the voltage can be predicted in advance, then the BMS may be able to control the discharge rate to keep the voltage above the cutoff level for as long as possible. The cell voltage imbalance problems can also be detected earlier with accurate battery voltage predictions [9].

It is important to note that there is a significant difference between the terminal and open circuit voltages of lithium-ion batteries. The former refers to the instantaneous voltage between the battery terminals, which can be easily measured. The latter is the steady-state voltage, called open circuit voltage (OCV), and it is related to the quantity of charge remaining in a battery.[2] To properly measure the OCV, the battery has to be relaxed for a long time, which can be impractical in real-time systems [10]. The principal intent of this work is to propose and evaluate a method for predicting the terminal voltage V as a linear combination of two parts: the steady-state OCV component, denoted by V_{OC}, and the transient component ΔV. Another important intent is to increase the explainability of the voltage prediction method. In this thesis, the *model explainability* refers to providing meaning between the input attributes and the model output. For example, to be detailed in the subsequent

---

[1] The SoC is the remaining battery charge typically expressed as a percentage of the battery capacity when it is fully charged. The SoH quantifies long-term capacity losses due to battery aging, and it is typically expressed as a percentage of the fully-charged battery capacity relative to that of the same battery when it was fresh, i.e., prior to its use or storage.

[2] The OCV concept arises from the basic thermodynamic considerations related to an electrochemical cell operation. Chapter 4 provides additional information on the OCV.

chapters, our model uses only the consumed charge information of the input to predict the V_{OC} component, thus enforcing the meaning that V_{OC} does not depend on the instantaneous battery current, which is a separate input attribute. The latter is used to predict the ΔV component (without using the consumed charge information), which highlights the link between the current and transient voltage dynamics.

1.3 Related Work

Nowadays, Deep Learning (DL) techniques are being broadly used for battery voltage modeling, SoC estimation, SoH estimation, and other battery-related characterization tasks [11][12][13][14]. A feedforward LSTM (Long Short Term Memory) network was used by Wang *et al.* [15] to predict SoC, where a sliding window was used for battery current filtering.[3] Partial differential equations and Laplace transformation were used by Gao *et al.* [16] to develop a transfer-function-based method, which was implemented in a real-time system to demonstrate its effectiveness. Liang *et al.* [17] modeled the terminal voltage using three different approaches, demonstrating that the data-driven DL model (based on the LSTM architecture) produced the most accurate results. However, the explainability of the model was not addressed, and the OCV component was not modeled separately. On the other hand, Shahriar *et al.* combined a Convolution Neural Network (CNN), a Gated Recurrent Unit (GRU), and an LSTM to create a hybrid model that was used to estimate the SoC based on measured terminal voltage, average voltage, instantaneous current, average current, and temperature. The model output was explained by calculating the importance of features using SHapley Additive exPlanations (SHAP) [18].

Zhu *et al.* [19] used a combination of statistical and machine learning methods to estimate the battery capacity from voltage relaxation. In that work, several statistical features were extracted using voltage relaxation, and machine learning methods were applied to estimate the capacity. This reference establishes the relations between the SoC and the OCV, which is highly valuable. Another OCV-SoC model using fractional calculus was proposed by Zhang *et al.* [20]. The experimental results demonstrated that the suggested OCV-SoC model had good performance under various conditions, satisfying the BMS accuracy requirements for the battery state estimation.

---

[3] LSTMs are discussed in more detail in Chapter 2.

1.4 Thesis Contribution and Organization

This thesis proposes an explainable DL model architecture with two wings for predicting the battery terminal voltage $V(t)$, where t represents time. The input to the first wing is the consumed battery charge, denoted by $C(t)$, and the output is the predicted OCV component $V_{OC}(t)$. The input to the second wing is the instantaneous current and temperature, denoted by $I(t)$ and $T(t)$, respectively. The output of the second wing is the predicted transient component $\Delta V(t)$. As mentioned earlier, expressing $V(t)$ in terms of steady-state $V_{OC}(t)$ and transient $\Delta V(t)$ is a key feature that makes the proposed model explainable. Also, we introduce a binary state input equal to $+1$ (charge) or -1 (discharge), reflecting the sign of the current $I(t)$. This enforces either adding or subtracting $\Delta V(t)$, when it is combined with $V_{OC}(t)$, which increases the model's explainability. In addition, we explore the use of an approximate four-parameter OCV equation based on [8], which is another novel aspect of this work. Overall, our voltage prediction model utilizes under 2.6K parameters, which is dominated by an LSTM portion in the second wing.

The rest of this thesis is organized as follows. Chapter 2 presents the background material, including the nature of the utilized dataset and the DL model building blocks. Chapter 3 describes the proposed model as well as the process of its training, validation, and testing, with quantitative analysis. Chapter 4 makes the case for replacing the multilayer perceptron (MLP) used in the first wing with an approximate OCV equation to further enhance the model's explainability. In Chapter 5, the discussion and comparison between the MLP-based and equation-based approaches to the V_{OC} component prediction are provided. In that chapter, we also compare our results to those reported in [17], where the task of battery voltage predictions was investigated as well. Finally, Chapter 6 gives a concluding summary of this thesis and outlines some directions for future work.

Chapter 2

Background

2.1 Dataset Description

Our voltage prediction model (detailed in the next chapter) has been trained, validated, and tested utilizing the dataset obtained from an LG 18650HG2 Li-ion battery with a 3 Ah LG HG2 cell [21]. Experimental measurements were conducted in a 0.23 m^3 thermal chamber, using a Digitron firing circuit rated at 75A and 5V as the battery tester. Different drive cycles (UDDS, HWFET, LA92, and US06) were randomly combined to create representative load profiles (drive cycles interleaved with charging cycles) for a single LG HG2 cell operating at ambient temperatures -20 °C, -10 °C, 0 °C, 10 °C, 25 °C, and 40 °C.

The UDDS drive cycle represents aggressive high-speed driving conditions with several sharp accelerations from 0 to over 50 mph and a roughly 350-second period of driving between 60 and 80 mph [22]. The Highway Fuel Economy Test (HWFET) drive cycle is intended to replicate highway driving conditions in order to assess fuel economy, emissions, and energy consumption in EVs. It emphasizes driving at high speeds (reaching 60 mph) with fewer stop-and-go occurrences than in urban settings [23]. The California Air Resources Board (CARB) created the LA92 drive cycle to mimic real-world urban driving conditions. It is widely used to assess the efficiency of EVs subjected to stop-and-go traffic and other urban driving patterns [24]. The U.S. Environmental Protection Agency (EPA) created the US06 drive cycle to replicate aggressive high-speed (up to 80 mph) driving conditions that include quick accelerations (up to 3.3 m/s^2) and decelerations. It resembles highway driving with aggressive manoeuvres, covering a total of 12.8 miles over 596 seconds [24].

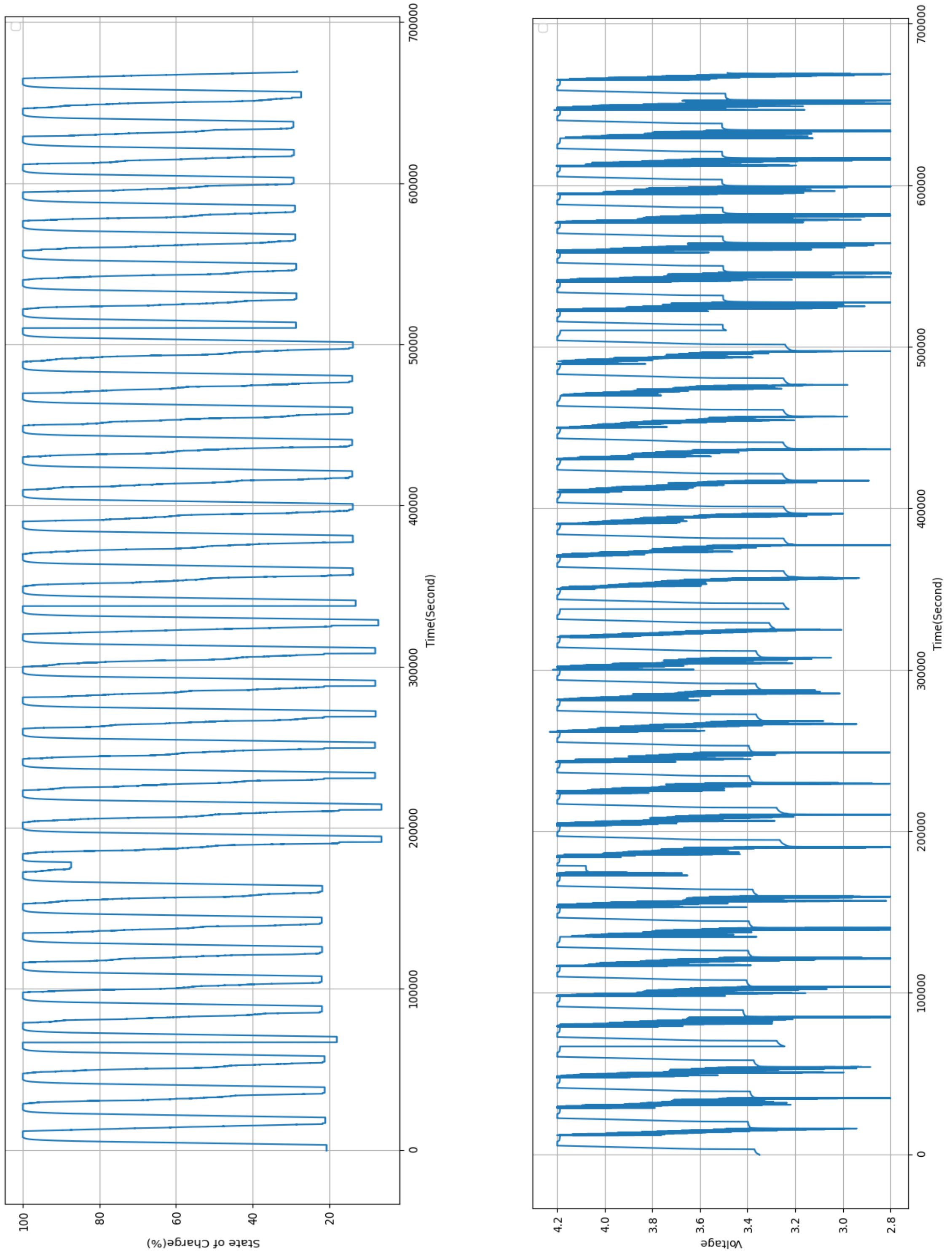

(a) SoC in %

(b) Terminal Voltage

Figure 2.1: Training Data: Measured SoC(t) and Terminal Voltage $V(t)$.

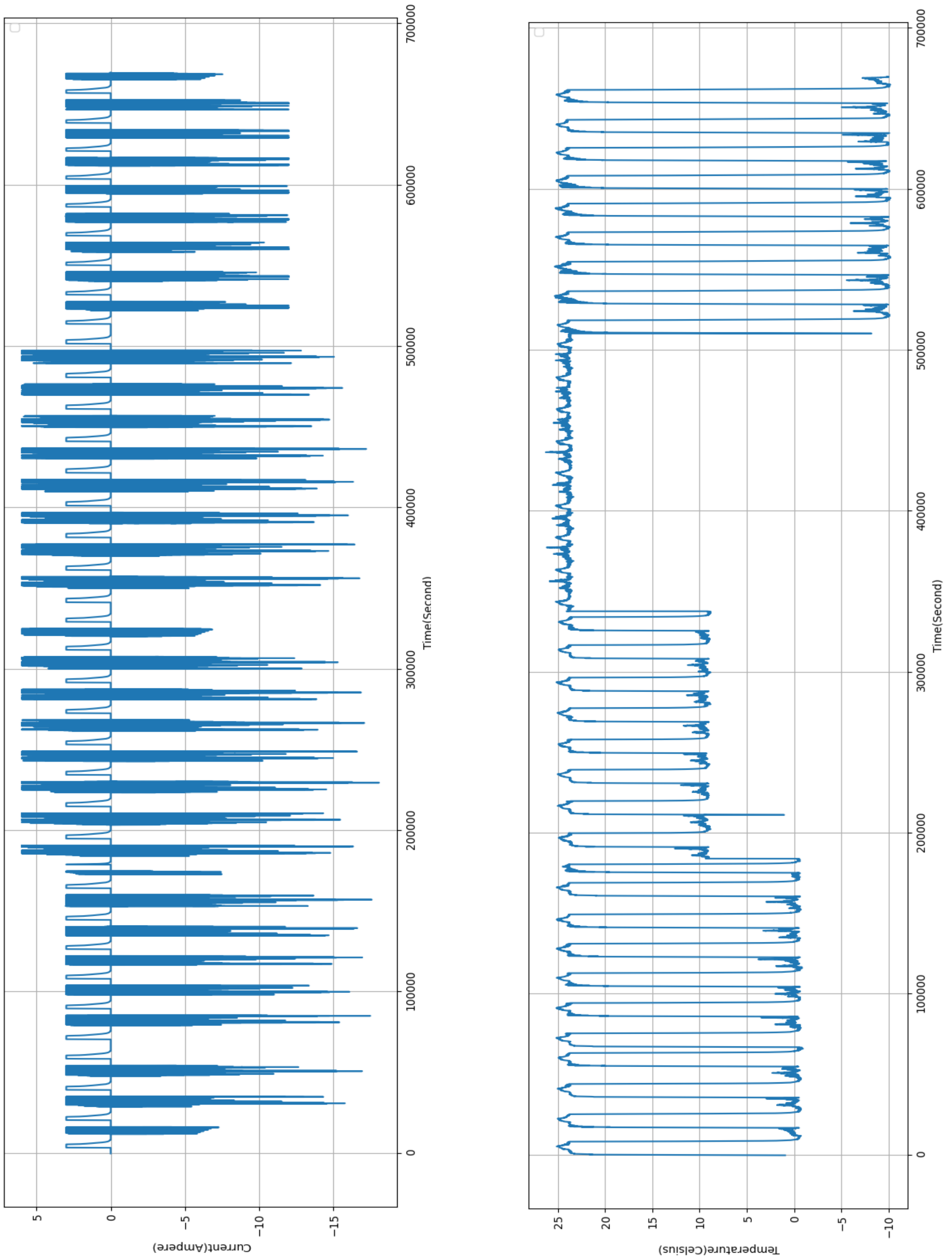

(a) Instantaneous Current

(b) Cell Temperature

Figure 2.2: Training Data: Measured Current $I(t)$ and Temperature $T(t)$.

After each applied drive cycle, the battery was charged at a 1C rate to 4.2 V with a cutoff current of 50 mA, maintaining a battery temperature of 25 °C. The consumed charge $C(t)$ was calculated using a simple Coulomb counter [25][26] that was reset prior to applying the next drive cycle in a load sequence. Further details on data logging and the test bench setup can be found in [27].

For this study, data from four ambient temperatures (-10 °C, 0 °C, 10 °C, and 25 °C) were utilized to form our training dataset. It includes four measured quantities sampled at a rate of 1 Hz: the terminal voltage $V(t)$, instantaneous current $I(t)$, cell temperature $T(t)$, and state of charge given by

$$\mathrm{SoC}(t) = \left(1 - \frac{C(t)}{C_{\mathrm{nominal}}}\right) \times 100\%. \tag{2.1}$$

Figures 2.1 and 2.2 show the individual plots of these quantities after concatenation across all four ambient temperature values. It should be noted that prior to training all measurements have been normalized to admit values between 0 and 1 only [21]. Letting x represent a quantity of interest, its normalized version is given by

$$x_{\mathrm{normalized}} = \frac{x - x_{\mathrm{min}}}{x_{\mathrm{max}} - x_{\mathrm{min}}}. \tag{2.2}$$

Our objective is to predict the terminal voltage $V(t)$ given the consumed charge $C(t)$, instantaneous current $I(t)$, and cell temperature $T(t)$. Our approach relies on building a deep learning model, but we also want to avoid making unexplained black-box predictions. To increase the explainability of our model output, we break down $V(t)$ into the OCV component $V_{OC}(t)$ and the transient component $\Delta V(t)$. These two components are to be predicted independently.

It is worth highlighting that the OCV can be thought of as the steady-state (stable, or equilibrium) battery voltage [10]. When the current flow is halted, and the battery is allowed to rest for a sufficiently long time, the terminal voltage effectively becomes equal to the OCV, which is related to the remaining battery charge. It important to note that the OCV itself (being related to the battery SoC) is not an accurate indicator of the remaining battery life, as the voltage cutoff crossing is also affected by the $\Delta V(t)$ responsive to the battery current $I(t)$ and temperature $T(t)$. This can be clearly observed in Figures 2.1, and 2.2, where the terminal voltage crosses the cutoff level at different SoC percentage levels, depending on the current and temperature profiles.

2.2 Deep Learning for Battery Voltage Modeling

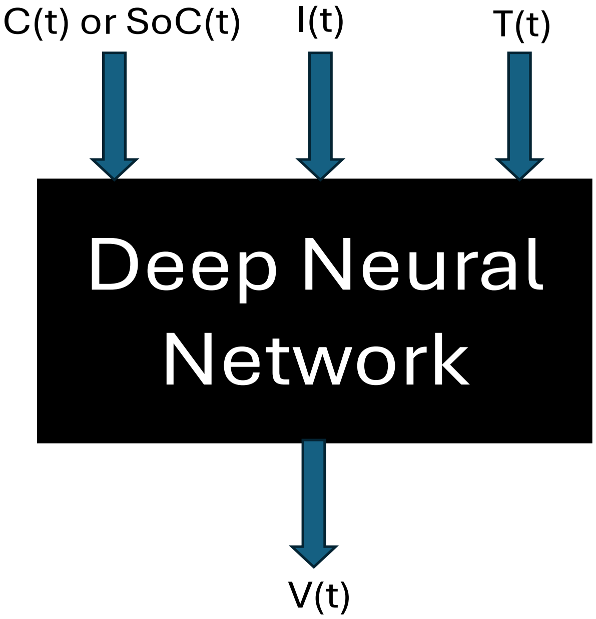

Figure 2.3: Conventional DNN-Based Approach to Voltage Modeling.

A typical deep neural network (DNN) model incorporates many layers. Many different types of layers have been proposed in the past, e.g., dense (fully connected) layers, convolution layers, and recurrent layers, no name a few [28]. When a DNN model produces a continuous output, it is called a regression model [29]. Such regression models have played a vital role in tackling the voltage modelling task [17][30][31].

In the context of the dataset described previously, the conventional approach to voltage modeling is illustrated in Figure 2.3. In [17], this approach was taken to build an LSTM-based model to predict the battery voltage using the measured current, temperature, state of charge as inputs. The reported model predictions were highly accurate (compared to non-DL alternatives); however, they were not explainable.

In the next two chapters, we present our proposed approach to building an explainable DNN model for the battery voltage predictions. The following sections introduce the basic model building blocks.

2.2.1 One-Dimensional Convolution

In this work, a one-dimensional (1D) convolutional layer was employed. The kernels of the 1D CNN layers are applied along the time dimension to extract temporal features [32]. We also perform so-called causal padding by adding zeros at the start of our sequential data, which helps with the early-time predictions.

2.2.2 Long Short Term Memory (LSTM)

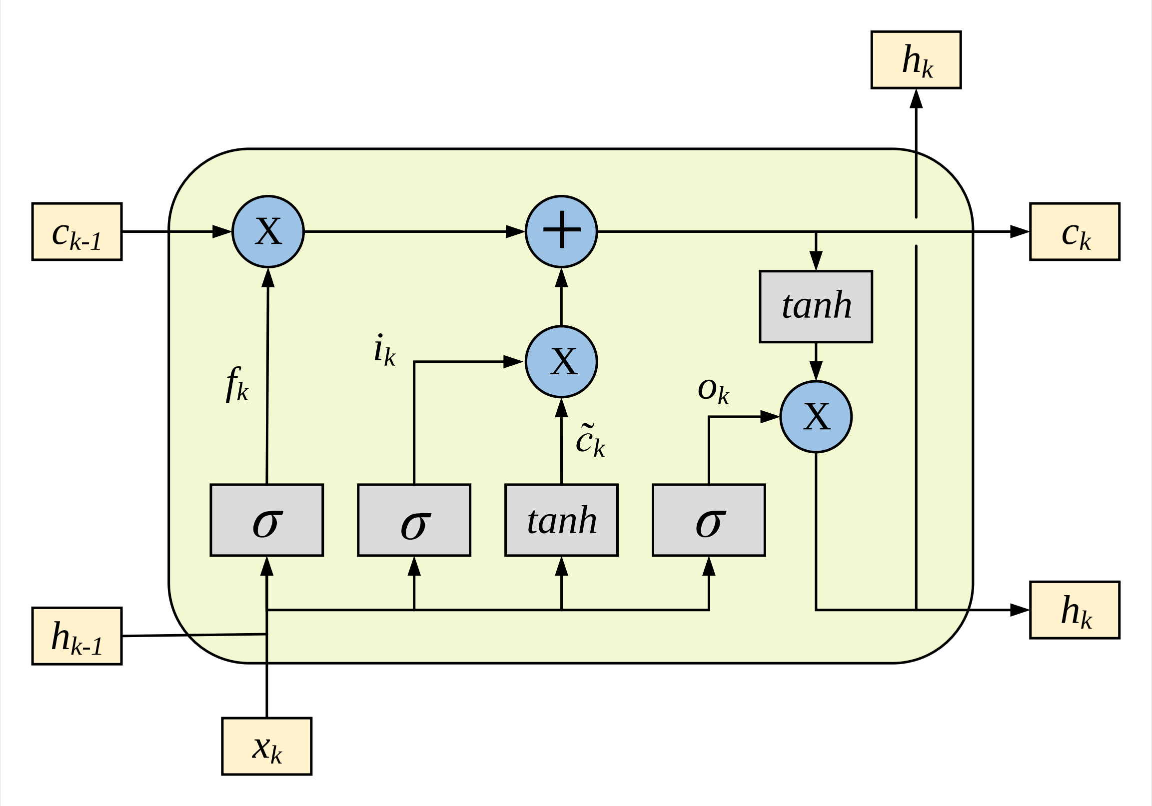

Figure 2.4: Internal Structure of LSTM Cell Used in This Thesis.

The LSTM cell structure was created expressly to avoid the issue of long-term dependency [33] and to remember the information over long periods. In Figure 2.4, the cell position is represented by k, while cell memory is represented by c_k. Each LSTM cell is built using three cells: forget, input, and output. Equation 2.3 defines the forget gate [27]:

$$f_k = \sigma(w_{fh} \cdot h_{k-1} + w_{fx} \cdot x_k + b_f), \tag{2.3}$$

where the output values between 0 and 1 are obtained by applying the sigmoid function, represented by the symbol σ. This gate determined how much the previous cell data c_{k-1} contributes to c_k. Here, w_{fh}, w_{fx}, and b_f define the weights and bias of the forget gate neuron. Symbols h_{k-1} and x_k stand for the preceding layer's hidden state and input data, respectively.

The new data are added to the cell memory c_k by the input gate. Equations (2.4) and (2.5) specify the two neurons of the input gate, where (w_{ih}, w_{ix}, b_i) and (w_{ch}, w_{cx}, b_c) are the corresponding weights and biases of the neurons:

$$i_k = \sigma(w_{ih} \cdot h_{k-1} + w_{ix} \cdot x_k + b_i) \tag{2.4}$$

$$\tilde{c}_k = \tanh(w_{ch} \cdot h_{k-1} + w_{cx} \cdot x_k + b_c). \tag{2.5}$$

Equation (2.6) shows how c_k is computed by combining the outputs of Equation (2.4) and (2.5):

$$c_k = f_k \cdot c_{k-1} + i_k \cdot \tilde{c}_k. \tag{2.6}$$

Equation (2.7) defines the output gate using the weights w_{oh}, w_{ox}, and bias b_o:

$$o_k = \sigma(w_{oh} \cdot h_{k-1} + w_{ox} \cdot x_k + b_o). \tag{2.7}$$

Then, c_k is converted to the value range between -1 and $+1$ by the *tanh* function. Finally, the result is multiplied by o_k to get h_k, as expressed by Equation (2.8):

$$h_k = o_k \cdot \tanh\left(c_k\right). \tag{2.8}$$

The primary issue with the earlier recurrent neural networks (RNNs) was that older inputs eventually become less relevant [34]. The LSTM resolves this long-term dependency issue by introducing the input and forget gates to regulate the cell memory.

2.2.3 Multilayer Perceptron (MLP)

An MLP is a type of artificial neural network (ANN) composed of an input layer, one or more hidden layers, and an output layer. Each layer consists of nodes (neurons), and each node is connected to every neuron in the subsequent layer, creating a dense network structure. The neurons in the hidden and output layers apply nonlinear activation functions (such as ReLU or sigmoid) to their weighted inputs, allowing the MLP to capture complex patterns and learn from data. Training involves optimizing weights through algorithms like backpropagation, minimizing a loss function by adjusting weights to reduce error. Figure 2.5 illustrates the architecture of a multilayer perceptron.

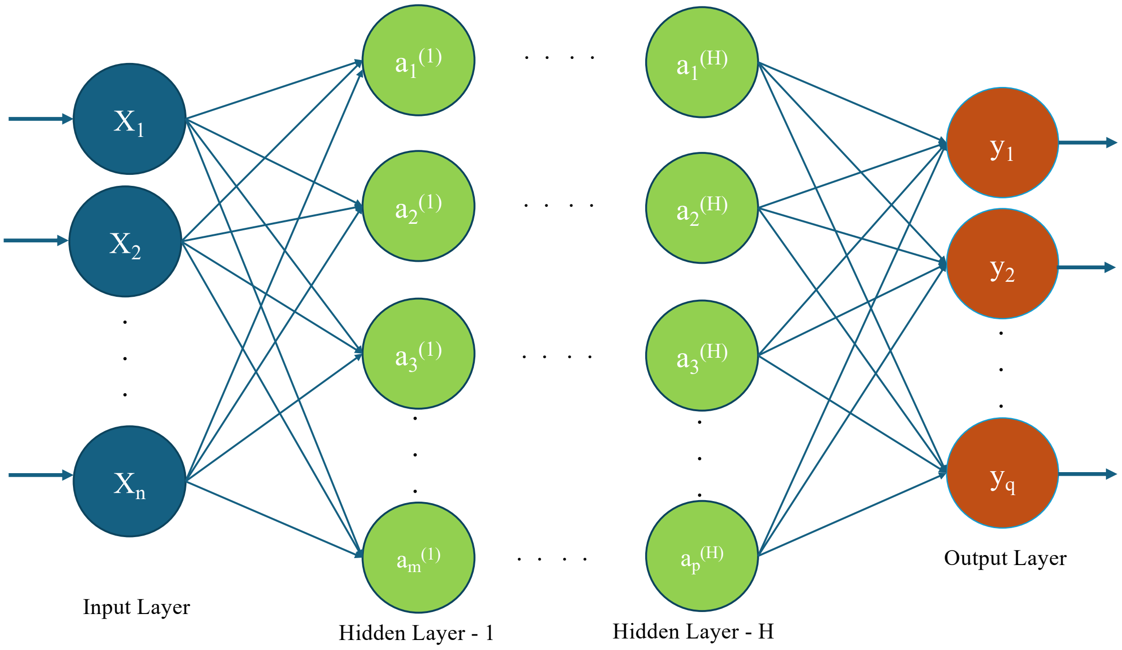

Figure 2.5: Multilayer Perceptron Architecture

Equation (2.9) specifies how the output h_j of a neuron a_j of a hidden layer is computed, where f, x_i, w_{ij}, and b_j denote the activation function, input from the previous layer, weights, and bias, respectively.

$$h_j = f\left(\sum_i x_i \cdot w_{ij} + b_j\right) \tag{2.9}$$

This work has also used a single-layer perceptron as a simple linear layer, i.e., it does not use any activation function [35].

Chapter 3

Proposed Explainable DNN Model

3.1 Model Building

Previous research demonstrated that OCV (i.e., the steady-state battery voltage at the absence of a discharge or charge current) can be obtained from the battery charge estimates [36]. Instantaneous current has no impact on the OCV, and hence we need to introduce a separate quantity ΔV representing the transient voltage component. Temperature should also be added as an input, because the battery operation is affected by it [37].

If we can predict V_{OC} and ΔV, then we can simply combine them to the terminal voltage. However, the available dataset does not contain direct measurements of V_{OC} and ΔV. In other words, we only have access to the terminal voltage measurements $V(t)$ as ground-truth labels. In fact, it is not practically feasible to measure $V_{OC}(t)$ and $\Delta V(t)$ separately. For example, to obtain the OCV value, one must halt the current flow and let the battery rest (before performing a measurement). This effectively modifies the battery load itself, represented by $I(t)$, under which we are trying to predict the terminal voltage $V(t)$.

This thesis proposes a double-winged model to resolve this problem. Its basic V-shaped architecture is shown in Figure 3.1, where wings A and B are tasked with predicting $V_{OC}(t)$ and $\Delta V(t)$, respectively. After that, a single-layer perceptron is used to compute the terminal voltage $V(t)$.

The single-layer perceptron output is given by Equation (3.1), where W_1 and W_2 are the corresponding weights of $V_{OC}(t)$ and $\Delta V(t)$, and b is the bias of the neuron. However, there is an extra input $S(t)$ that represents the sign of the battery current

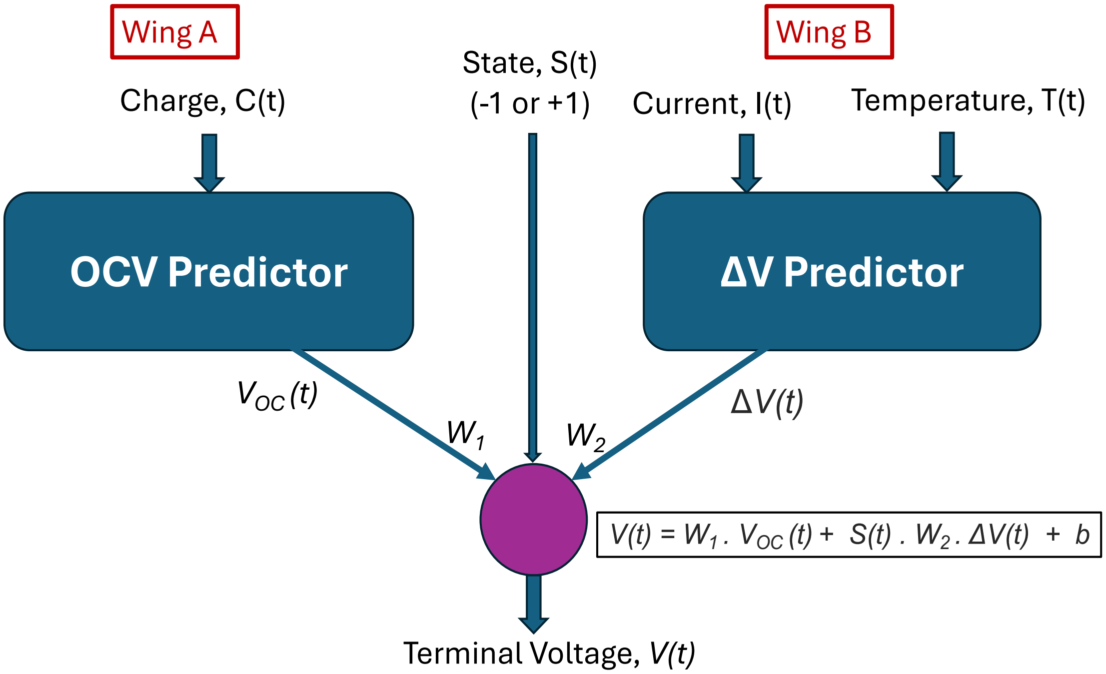

Figure 3.1: V-Shaped Double Winged Model Architecture

$I(t)$, and it is used as a multiplier for W_2. During charging, the sign of W_2 will be positive and during discharging, the sign of W_2 will be negative. This is done to enhance the model's explainability by guiding the single-layer perceptron to add $\Delta V(t)$ to $V_{OC}(t)$ when $I(t)$ is positive (charging) or subtract $\Delta V(t)$ from $V_{OC}(t)$ when $I(t)$ is negative (discharging).

$$V(t) = W_1 \cdot V_{OC}(t) + S(t) \cdot W_2 \cdot \Delta V(t) + b \tag{3.1}$$

While the parameters W_1, W_2, and b are introduced here for the sake of generality, in this work we fix their respective values to 1, 1, and 0 for simplicity. In other words, the single layer perception was made non-trainable during the backpropagation process.

3.1.1 Wing A: OCV Predictor

An MLP is used as the OCV predictor. Its input is the consumed battery charge $C(t)$ obtained by Coulomb counting the battery current values $I(t)$ over time. We should mention that for convenience the $C(t)$ information is internally represented by SoC(t) according to Equation (2.1). After the input layer, there are two hidden layers, referred to as Dense Layers 1 and 2, producing 16 and 4 neuron outputs, respectively. Their activation function is the Rectified Linear Unit (ReLU) that works as follows. If the input is positive, the ReLU directly outputs that input value; otherwise, it outputs zero. Because of its simplicity and capacity to alleviate the vanishing gradient issue, it is extensively employed in neural networks [38]. Finally, there is an output layer that simply computes the linear combination of its inputs to produce $V_{OC}(t)$. The architecture is summarized in Table 3.1. A total of 105 parameters have been used to build the OCV predictor.

Table 3.1: OCV Predictor Configuration

Layer	**Output Size**	**No. Parameters**
Input Layer	(None, 1)	0
Dense Layer 1	(None, 16)	32
Dense Layer 2	(None, 4)	68
Output Layer	(None, 1)	5

3.1.2 Wing B: ΔV Predictor

Table 3.2: ΔV Predictor Configuration

Layer	**Output Size**	**No. Parameters**
Input Layer	(None, 1, 2)	0
1D Conv Layer	(None, 1, 16)	272
LSTM	(None, 16)	2112
Flatten Layer	(None, 16)	0
Dense Layer	(None, 8)	136
Output Layer	(None, 1)	9

An LSTM-based model has been used as the ΔV predictor. To extract the essential features from the data, the first layer performs 1D convolutions with 16 filters having the kernel size of 8. Causal padding is also applied to ensure that the output at any time step only depends on the current and past time steps, without considering future time steps. This is accomplished by adding zeros at the start of the sequential data, so that the predictions at the early time steps are made easier [18]. After that, an LSTM layer has been used, comprised of 16 cells. It is followed by the Flatten layer that makes the tensors one-dimensional. Then, a fully connected (dense) layer produces 8 neuron outputs, and finally, the linear output layer produces $\Delta V(t)$. The architecture is summarized in Table 3.2. A total of 2,529 parameters were used to build the ΔV predictor.

3.2 Custom Loss Function

The primary loss function utilized during the training process is the mean absolute error (MAE) specified below, where $\hat{V}(t)$ and $V(t)$ refer to the predicted and true (measured) voltage values, respectively, over N consecutive time instances under consideration during training:

$$\mathrm{MAE} = \frac{1}{N}\sum_{t=1}^{N}\left|\hat{V(t)} - V(t)\right|. \tag{3.2}$$

To facilitate the overcharge and over-discharge protection, we introduce two extra terms to the MAE loss. Suppose the battery is charging and the true voltage is over the upper limit of the voltage range, but the predicted voltage is lower than the true voltage. This situation indicates that the battery may be close to being overcharged, but the model's output suggests otherwise. On the other hand, if the battery is discharging and the true voltage is lower than the lower limit of the voltage range but the predicted voltage is higher than the true voltage, it indicates that the battery may be close to being over-discharged, but the model's output suggests otherwise. If any of these two cases happen, we add either overcharge penalty (OCP) and over-discharge penalty (ODP).

$$OCP = \begin{cases} Penalty, & \text{if } I(t) \geq 0 \text{ and } V(t) \geq UpperLimit \text{ and } \hat{V}(t) < V(t) \\ 0, & \text{otherwise} \end{cases}$$

$$ODP = \begin{cases} Penalty, & \text{if } I(t) < 0 \text{ and } V(t) \leq LowerLimit \text{ and } \hat{V}(t) > V(t) \\ 0, & \text{otherwise} \end{cases}$$

Then, the total loss function can be defined as

$$Loss = MAE + ODP + OCP. \tag{3.3}$$

In this work, the upper limit and the lower limit have been set to 95% and 5%, respectively. The *Penalty* amount has been set to 0.1 for both OCP and ODP.

3.3 Training Details

In the training dataset, there are a total of 6,69,956 data points at four ambient temperatures (-10 °C, 0 °C, 10 °C, and 25 °C). On the other hand, the 39,293 data points at -10 °C are used as the validation set. The reason for choosing the -10 °C data points is that at low temperatures it is harder to predict the battery voltage accurately [17]. Adam (Adaptive Moment Estimation) has been employed as the optimizer. It leverages momentum to speed up convergence and adjusts the learning rate for every parameter, combining the advantages of AdaGrad and RMSProp. To stabilize early updates, Adam computes moving averages of the gradient (first moment) and squared gradient (second moment), adding bias correction. Since it quickly converges and is adaptive, it is effective, memory-light, and frequently utilized in training [39]. The model was trained over 40 epochs using the TensorFlow 2.6.0 framework and an NVIDIA RTX3060 GPU. It took 1 hour and 3 minutes to complete the training.

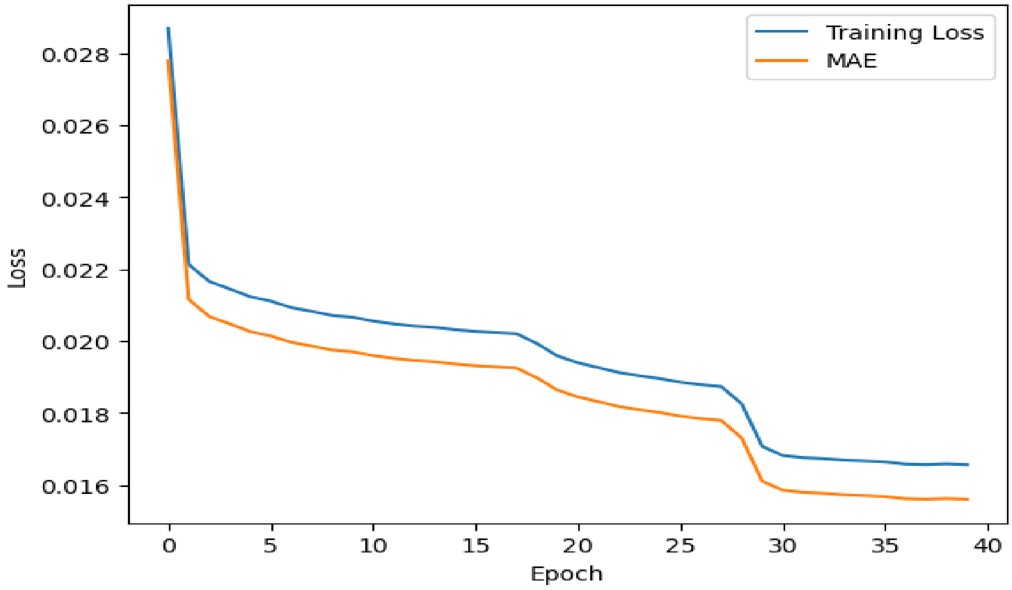

Figure 3.2: Custom Training Loss vs Mean Absolute Error

The validation dataset plays a vital role in finding the optimized model. The validation loss has been calculated after every training epoch. It has been observed that the minimum validation error occurs at the 24th epoch, and the weights of the model have been saved using the callback feature of TensorFlow. The training and validation MAE at the 24th epochs were 0.018 and 0.066, respectively. Although the training loss kept decreasing, the validation loss did not improve. Hence, the weights of the 24th epoch were chosen as the final weights.

The custom loss function added an extra penalty for overcharge and overvoltage protection. In Figure 3.2, the custom loss and the mean absolute error are plotted. As one can see, the custom loss is higher than the MAE, which indicates that the OCP and OCP contributions are present.

3.4 Test Results

After the training process, the model has been tested on the data points at four ambient temperatures (-10 °C, 0 °C, 10 °C, and 25 °C). Three discharging drive cycles (UDDS, LA92, and US06) and two constant-current charging cycles were included in the test data. The Mean Absolute Percentage Error (MAPE) and Root Mean Square Percentage Error (RMSPE) for each ambient temperature are listed in Table 3.3, and the bar chart is shown in Figure 3.3. Since we have used an MLP as the OCV predictor, the network presented in this chapter is referred to as the "MLP-based model". The predicted voltage and the ground truth are plotted in Figures 3.4, 3.6, 3.8, and 3.10 (along with the errors curves). The corresponding plots of the $V_{OC}(t)$ and $\Delta V(t)$ predictions are shown in Figures 3.5, 3.7, 3.9, and 3.11.

Table 3.3: Summary of Test Results for MLP-Based Model

Ambient Temp.	**MAPE (%)**	**RMSPE (%)**	**Worst Case Overestimate (V)**	**Worst Case Underestimate (V)**
-10 °C	0.67	1.28	0.50	0.27
0 °C	0.67	1.13	0.38	0.15
10 °C	0.82	1.22	0.31	0.18
25 °C	0.70	1.17	0.23	0.11

At -10 °C and 0 °C, the MAPE is the same and equal to 0.67%. However, the RMSPE is larger, reaching 1.28% and 1.13%, respectively. The MAPE rises to 0.82% at 10 °C and 0.70% at 25 °C. The RMSPE at 10 °C and 25 °C is equal to 1.22%

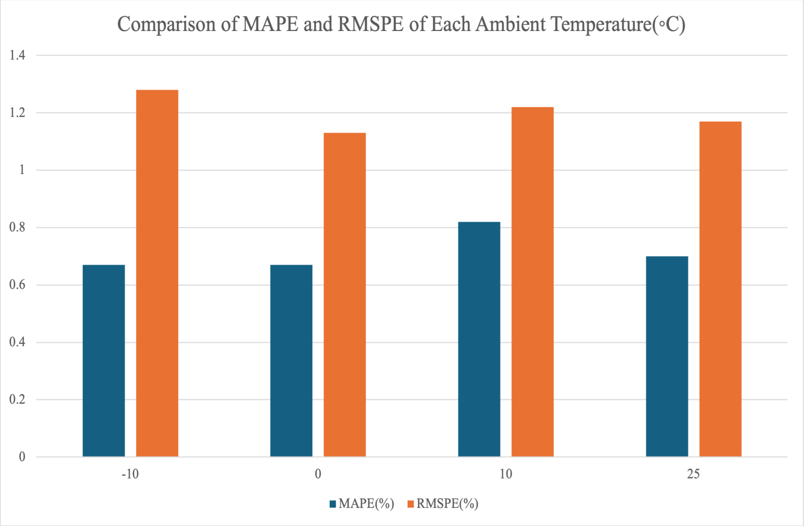

Figure 3.3: MAPE and RMSPE of MLP-Based Model

and 1.17%, respectively. While slightly higher at -10 °C and 0 °C, these values still indicate that the overall prediction accuracy of the proposed model is high.

At 0 °C, the model has the lowest RMSPE (1.13%) and MAPE (0.67%), indicating that the model performs best at this ambient temperature (compared to the other four). At -10 °C, the model performs marginally worse, giving the RMSPE of 1.28%, while the MAPE is still low at 0.67%. Overall, at both low and high temperatures, the model achieves a high degree of accuracy, which makes it well-suited for applications where the ambient temperature may vary from -10 °C to 25 °C.

Table 3.3 additionally displays the worst-case voltage overestimation and underestimation errors. The worst-case overestimation error drops dramatically with increasing temperature, from 0.50 V at -10 °C to 0.23 V at 25 °C. The worst-case underestimation error exhibits a similar downward trend, peaking at -10 °C (0.27 V) and falling to its lowest at 25 °C (0.11 V). The model's capacity to forecast voltages appears to improve with increasing temperature, as evidenced by the fact that both overestimation and underestimation errors decrease with rising temperatures. It should also be mentioned that across all temperatures, the worst-case overestimation errors are significantly higher than the worst-case underestimation errors.

The primary observation from the test results (see Figures 3.4, 3.6, 3.8, and 3.10) is that the error is very low during charging cycles and relatively high during drive cycles. The latter is a harder case for the model to handle, as the drive cycles are characterized by significantly varying battery currents, including both discharging and

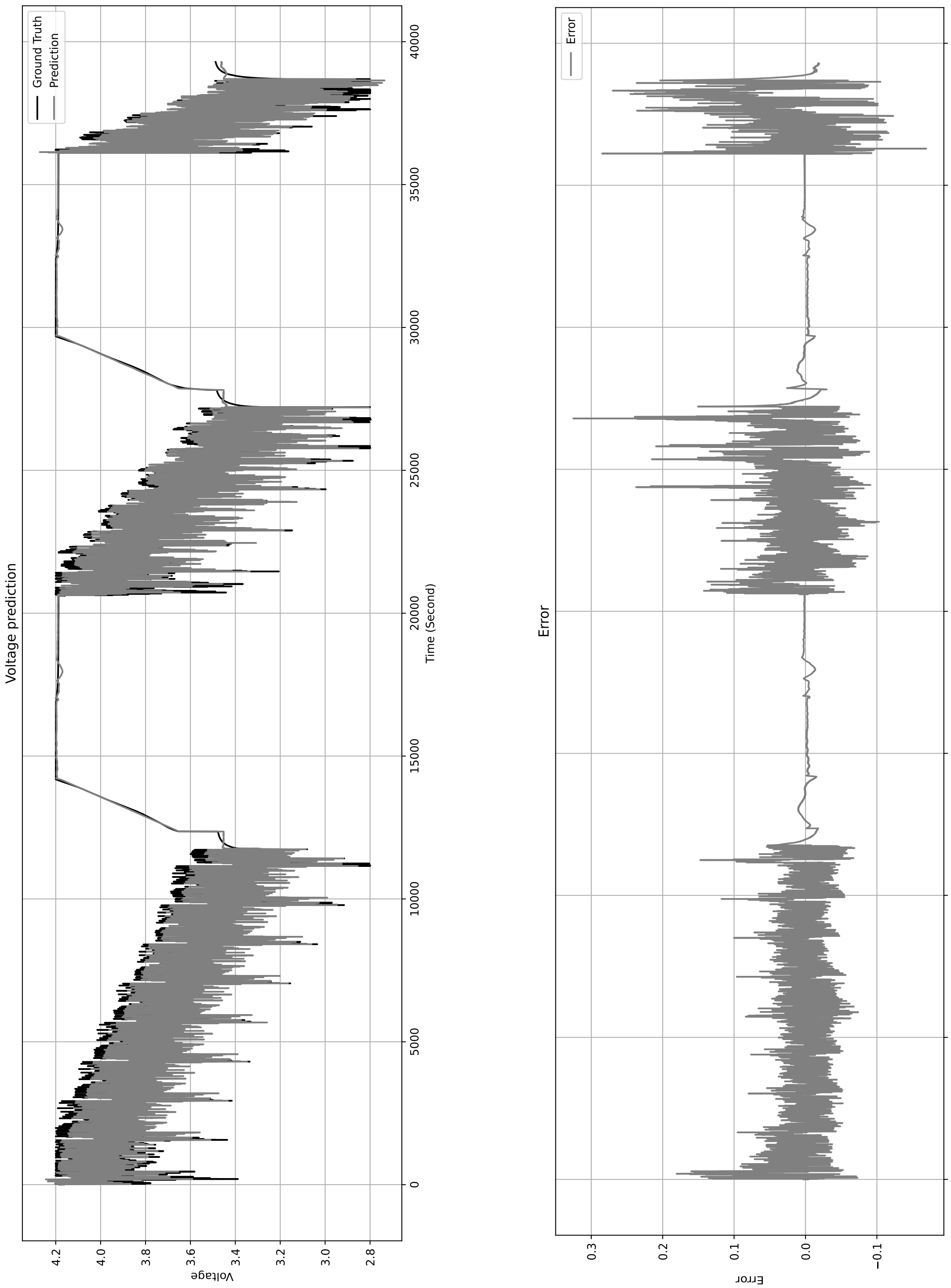

(a) Predicted Voltage vs Ground Truth (b) Error (Predicted Voltage - Ground Truth)

Figure 3.4: MLP-Based Model, Test Results at -10°C

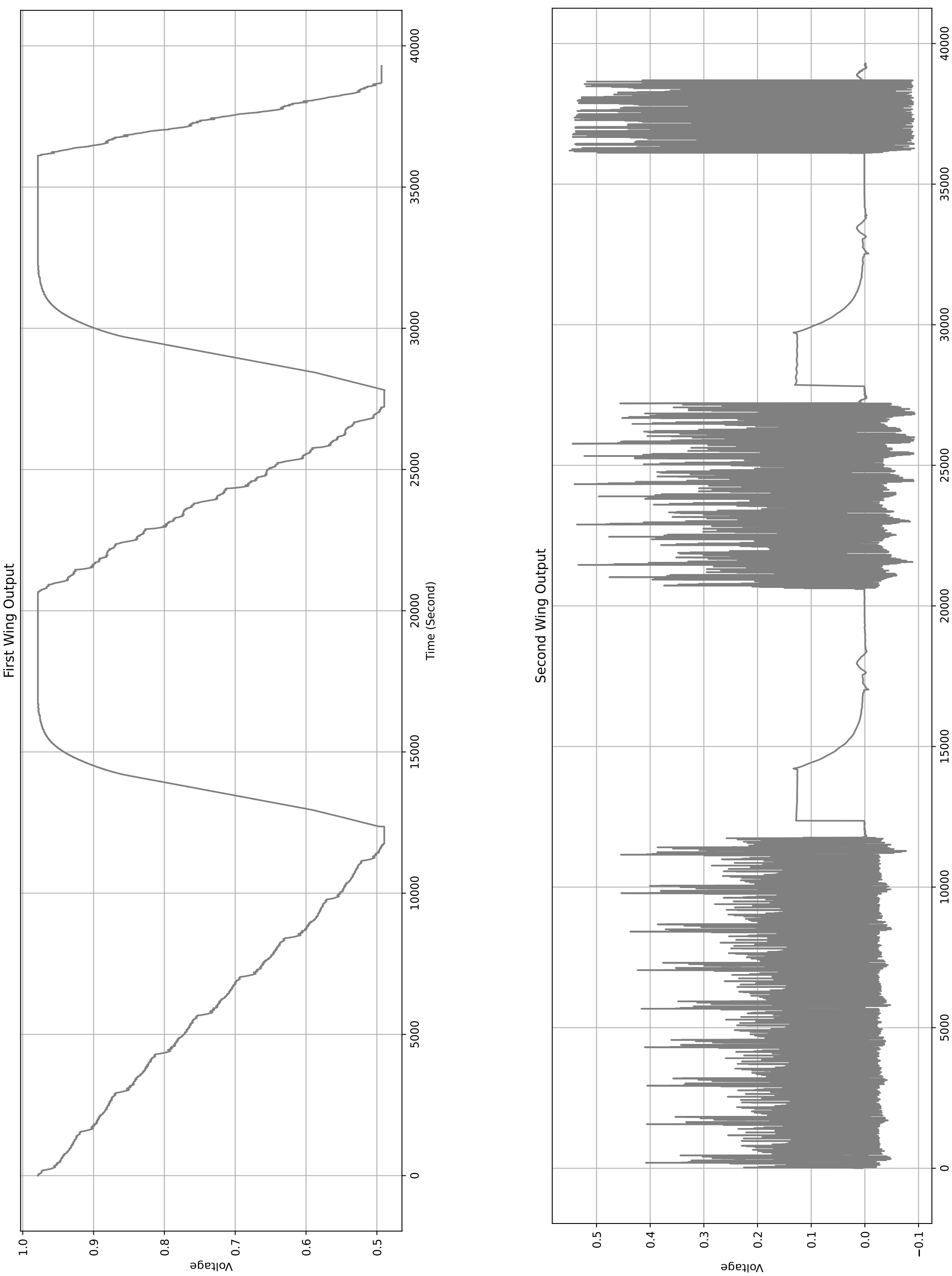

(a) First Wing Output

(b) Second Wing Output

Figure 3.5: Individual Wing Outputs of MLP-Based Model, -10°C Data.

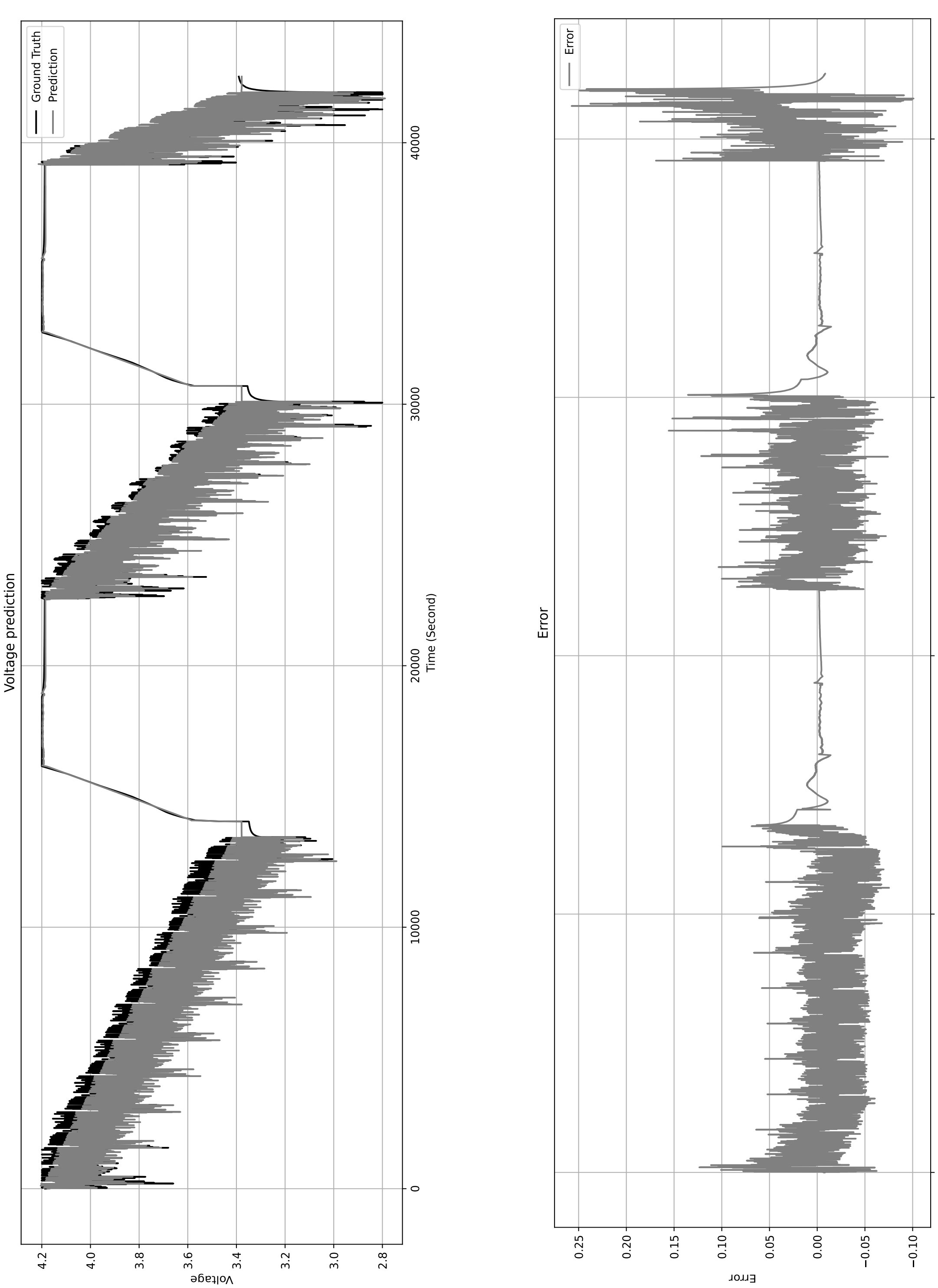

(a) Predicted Voltage vs Ground Truth

(b) Error (Predicted Voltage - Ground Truth)

Figure 3.6: MLP-Based Model, Test Results at 0°C

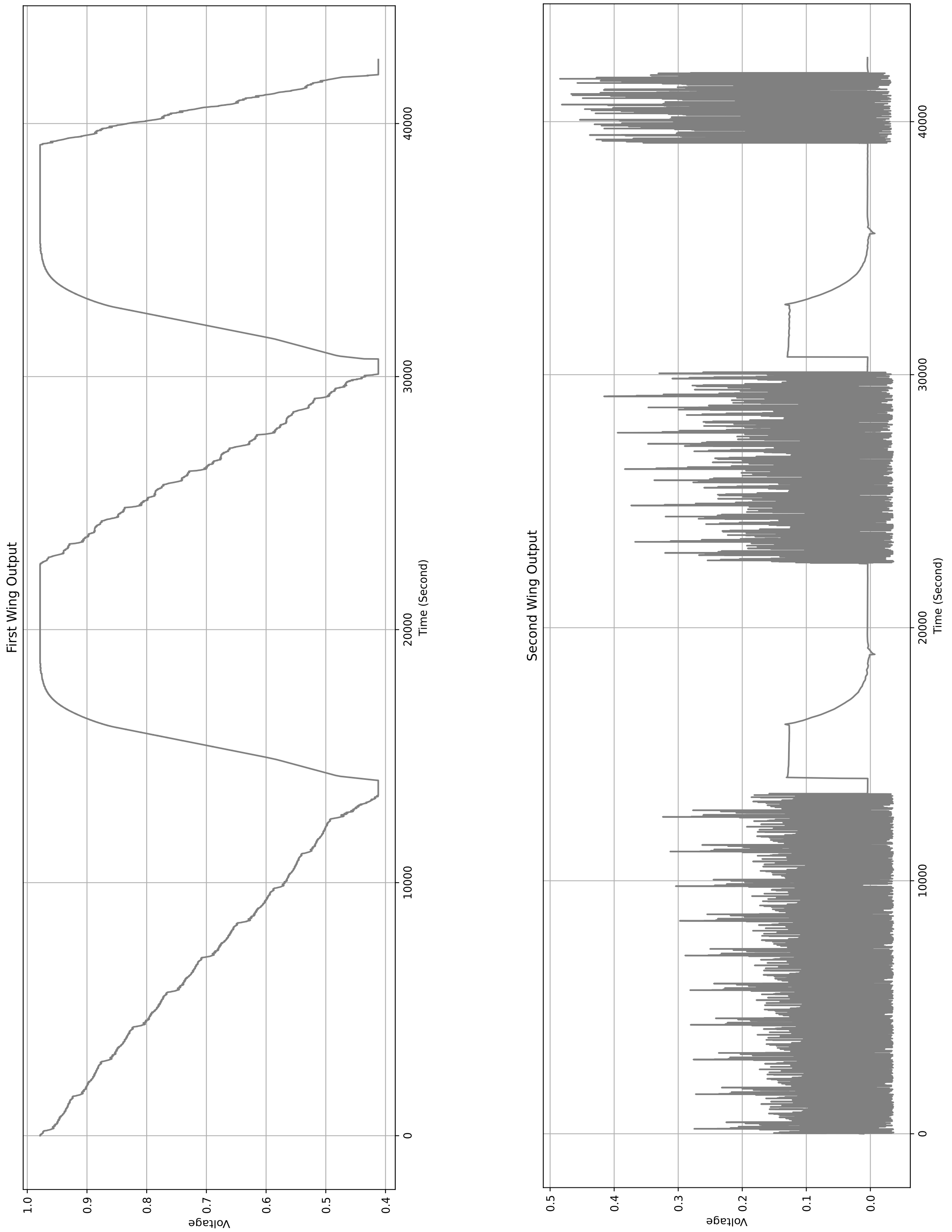

(a) First Wing Output

(b) Second Wing Output

Figure 3.7: Individual Wing Outputs of MLP-Based Model, 0°C Data.

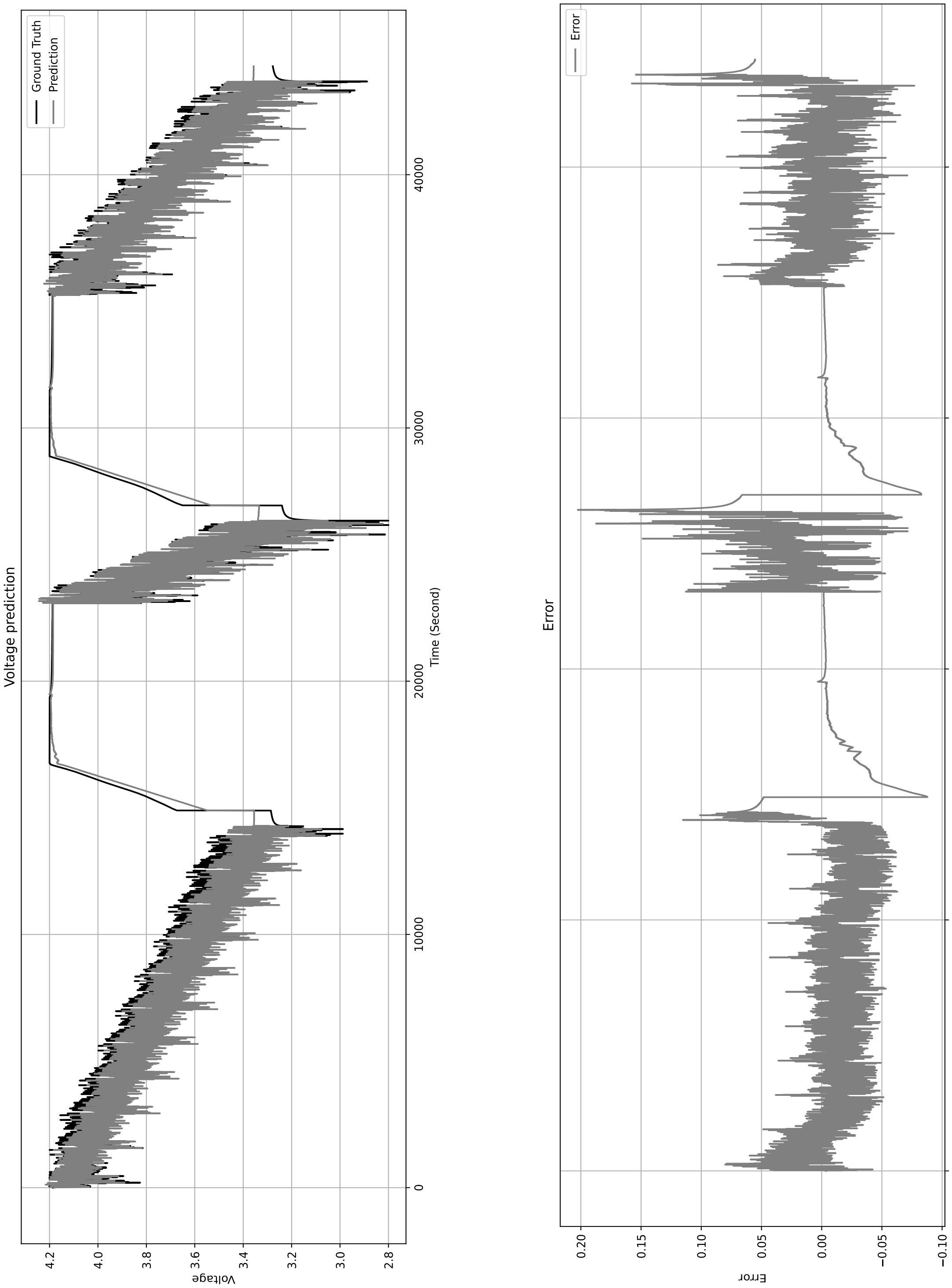

(a) Predicted Voltage vs Ground Truth

(b) Error (Predicted Voltage - Ground Truth)

Figure 3.8: MLP-Based Model, Test Results at 10°C

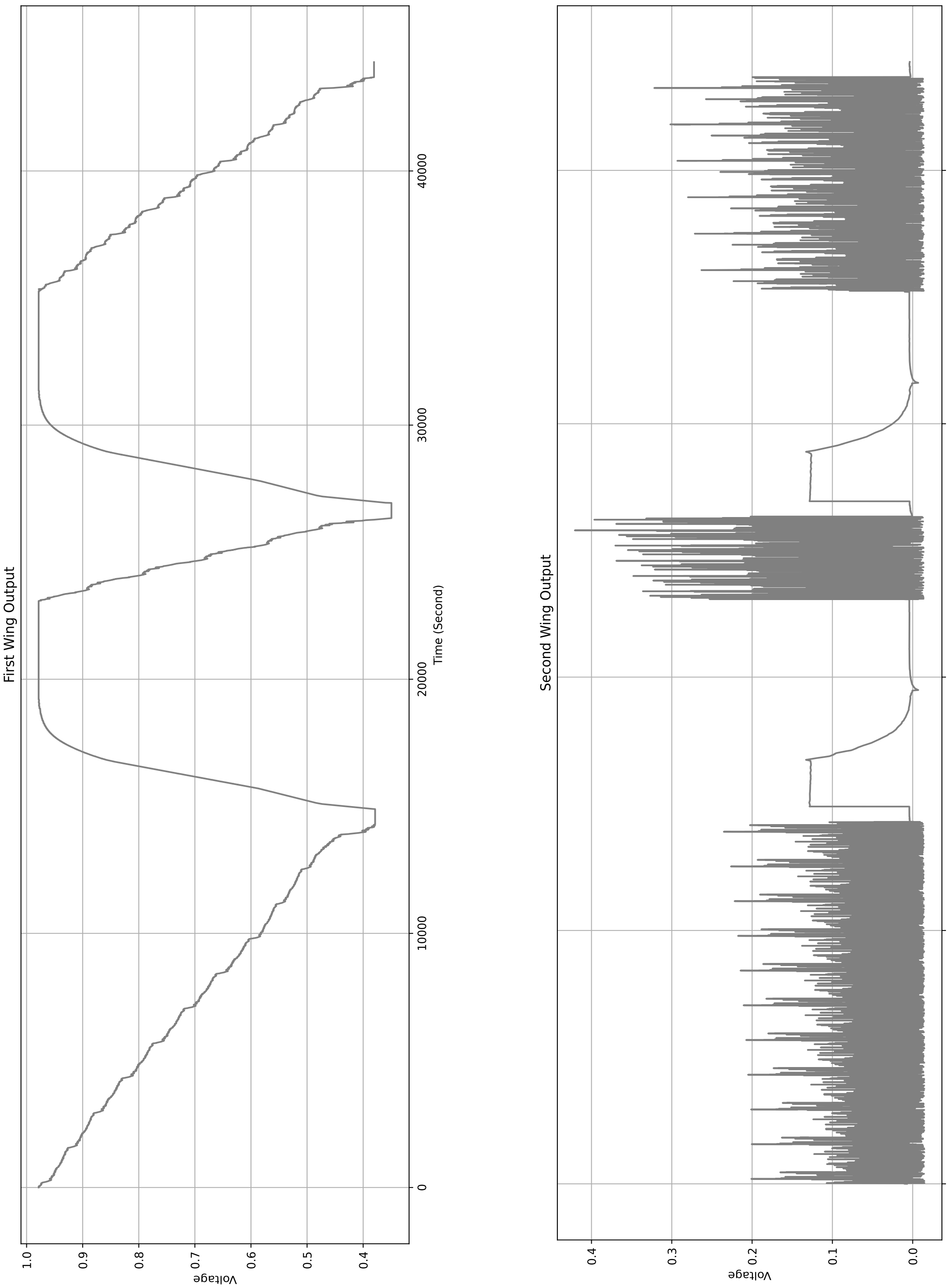

(a) First Wing Output

(b) Second Wing Output

Figure 3.9: Individual Wing Outputs of MLP-Based Model, 10°C Data.

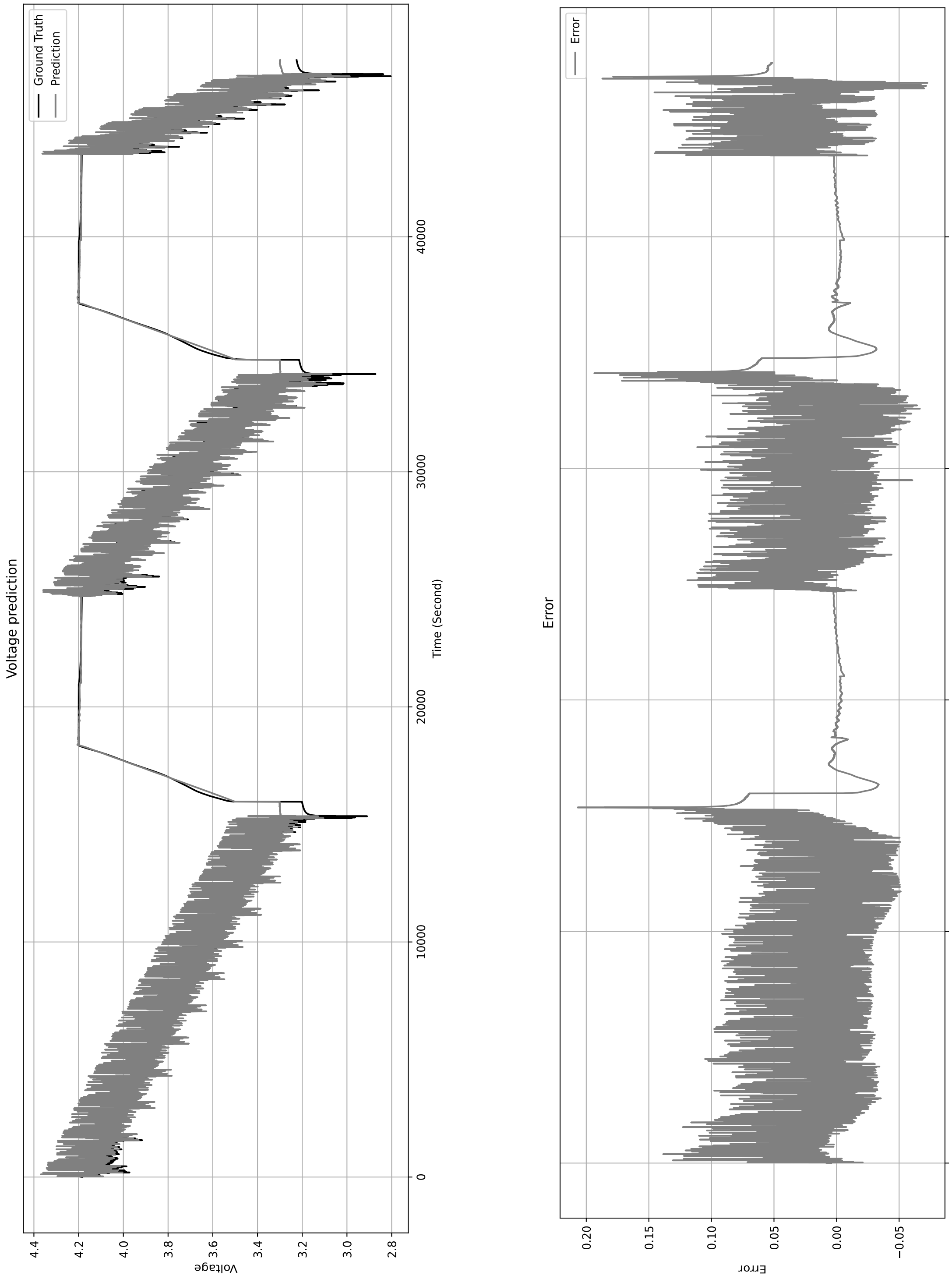

(a) Predicted Voltage vs Ground Truth

(b) Error (Predicted Voltage - Ground Truth)

Figure 3.10: MLP-Based Model, Test Results at 25°C

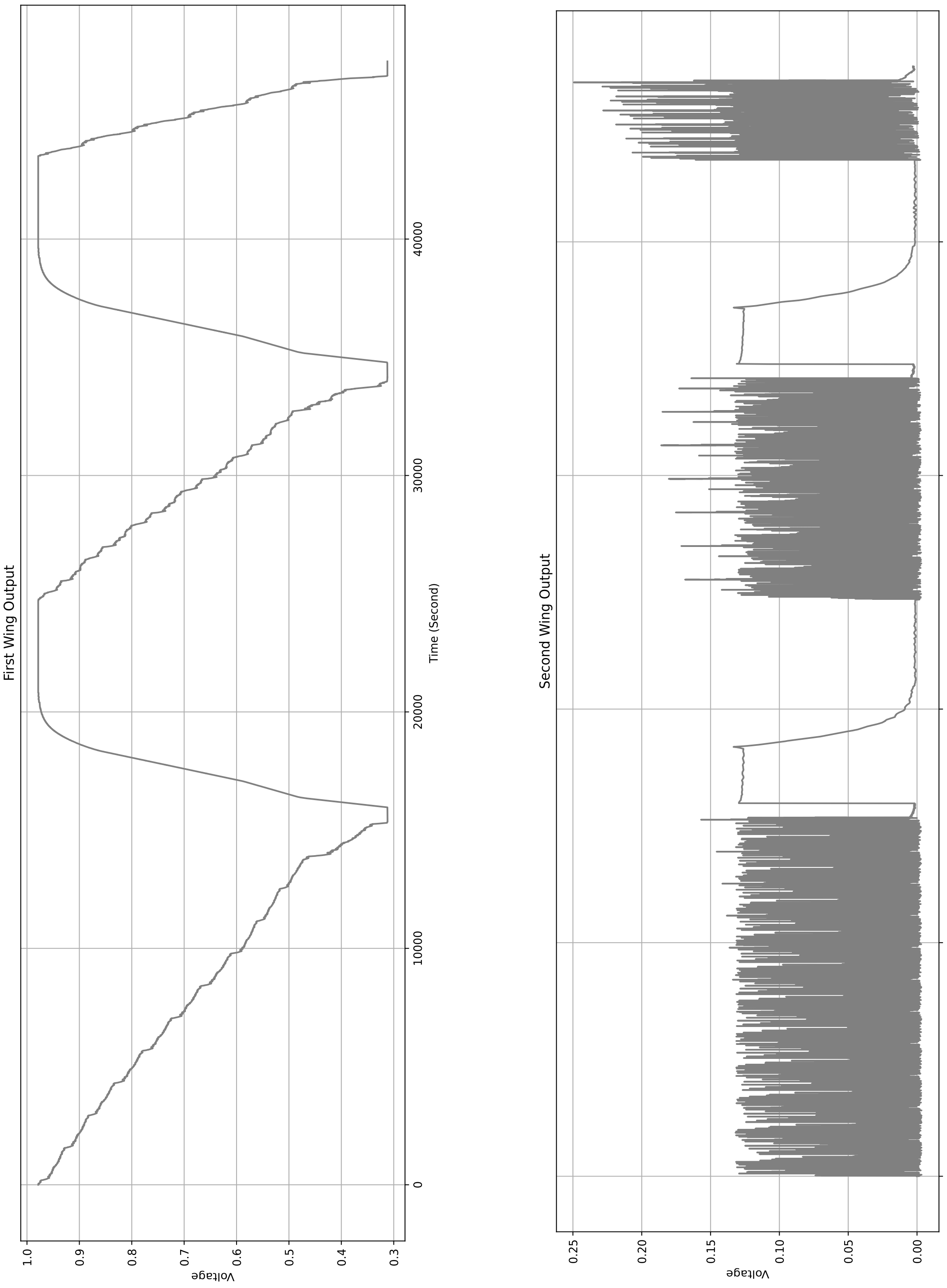

(a) First Wing Output

(b) Second Wing Output

Figure 3.11: Individual Wing Outputs of MLP-Based Model, 25°C Data.

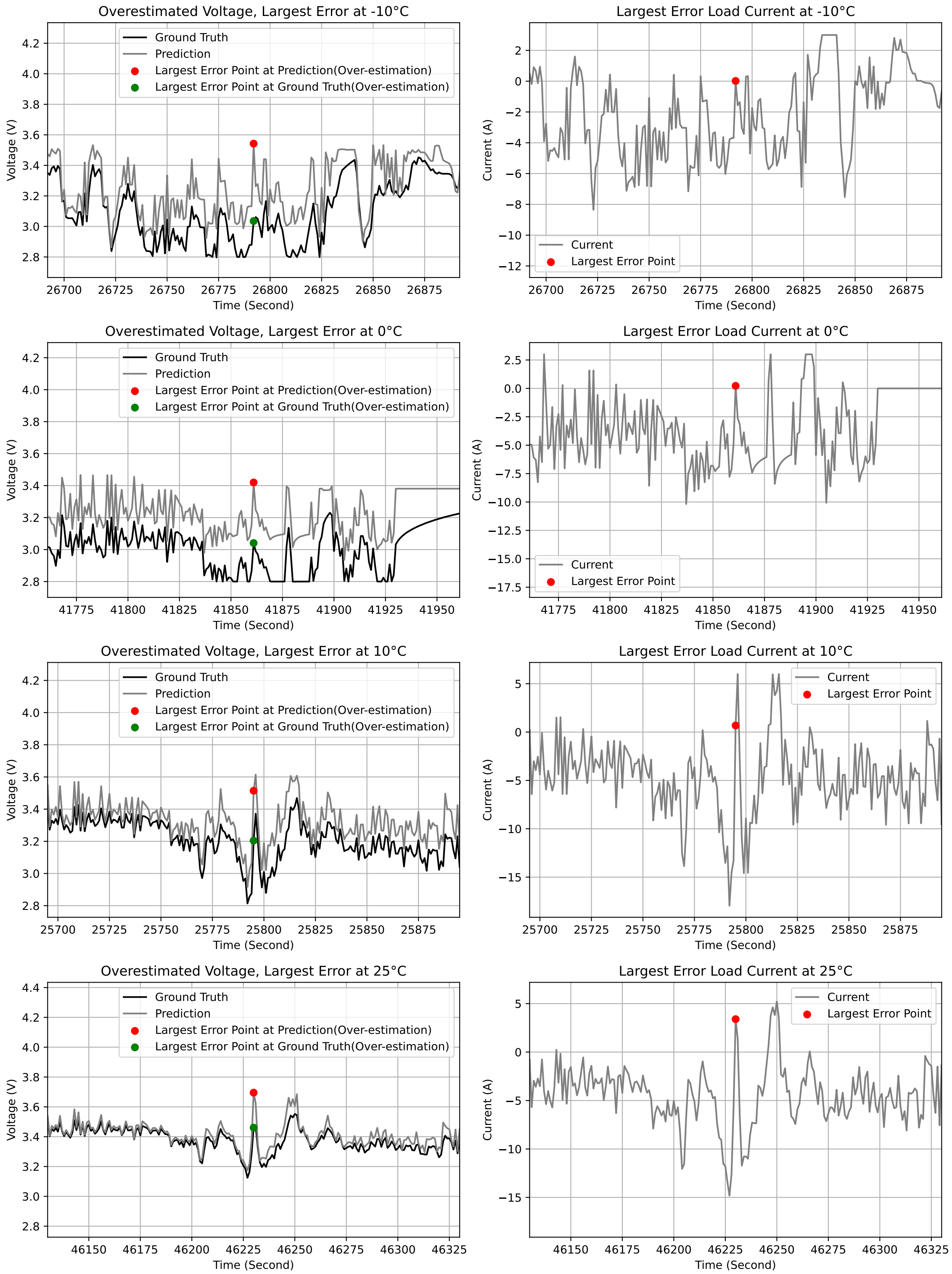

Overestimated Voltage, Largest Error at -10°C

Largest Error Load Current at -10°C

Overestimated Voltage, Largest Error at 0°C

Largest Error Load Current at 0°C

Overestimated Voltage, Largest Error at 10°C

Largest Error Load Current at 10°C

Overestimated Voltage, Largest Error at 25°C

Largest Error Load Current at 25°C

Figure 3.12: Worst-Case Voltage Overestimation by MLP-Based Model

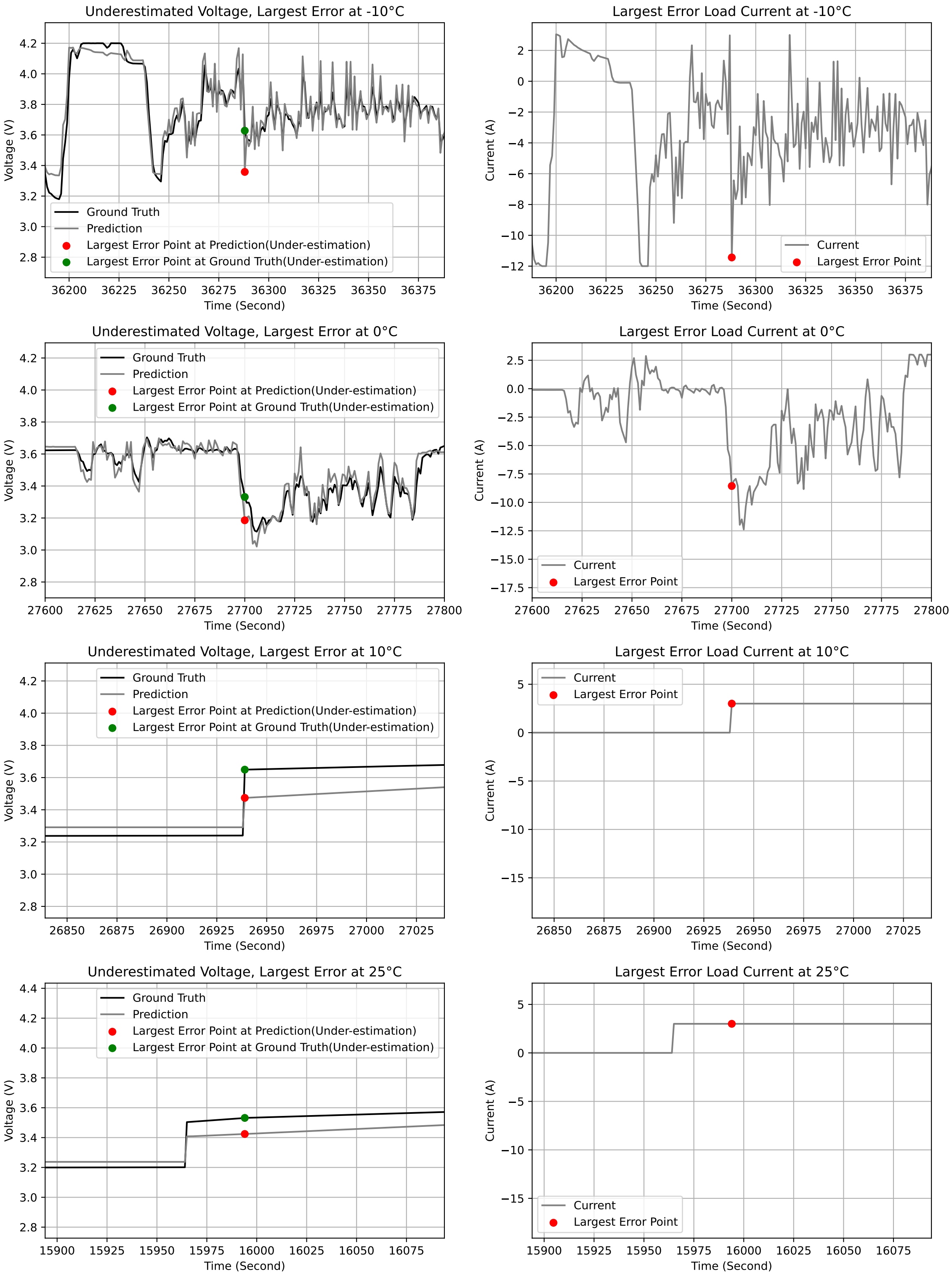

Figure 3.13: Worst-Case Voltage Underestimation by MLP-Based Model

charging intervals due to regenerative braking [40]. In the dataset, the discharging current is negative, and the charging current is positive. Though most of the data points in the drive cycles are negative, there are some positive currents as well due to regenerative braking.

Observing the output of the first wing at each temperature, its shape appears to be consistent with the expected behavior of the OCV (see Figures 3.5, 3,7, 3.9, and 3.11). Recall that V_{OC} is predicted based on the Coulomb-counted charge information only. During drive cycles, V_{OC} gradually decreases and despite regenerative braking, there is little fluctuation. During charging cycles, the predicted OCV curve is even smoother, as the charging currents do not vary dramatically. On the other hand, the second wing's output ΔV, predicted partly based on the instantaneous current, exhibits significant fluctuations representing transient voltage deviations from the OCV. Combining V_{OC} and ΔV yields accurate predictions of the terminal voltage, which supports our claim of the model explainability.

The worst-case overestimation and underestimation error sections are depicted in Figures 3.12 and 3.13. The battery current within these sections is plotted as well for reference. The difference between the predicted voltage and ground truth is much higher in overestimation cases than underestimation cases. Interestingly, in the overestimation cases, the shape of the predicted voltage and ground truth look somewhat similar, suggesting the presence of a dynamic bias. This phenomenon may be worth exploring further, which is one of possible directions of future work outlined in Chapter 6.

Chapter 4

Alternative Model with Equation-Based OCV Predictor

4.1 Approximate OCV Equation

In the previous chapter, our proposed battery voltage model used a 105-parameter MLP as the OCV predictor. Here, we replace the MLP with a 4-parameter OCV equation, which is a special case of an approximate non-DL voltage model from [8]. This equation is shown below, and its parameters are denoted by V_o, φ, α_n, and α_p.

$$V_{OC}(t) = V_o - \varphi \cdot \ln\left(\frac{\alpha_n + C(t)}{\alpha_p - C(t)}\right) \tag{4.1}$$

Note that $V_{OC}(t)$ in Equation (4.1) is a function of the consumed battery charge $C(t)$, and recall that the OCV-predicting MLP from Chapter 3 also uses $C(t)$ as the input. In other words, both Equation (4.1) and the MLP in question are both aiming to capture a mapping from $C(t)$ to $V_{OC}(t)$. Since the equation-based approach is more explainable, we argue that the alternative model presented here is better in terms of its explainability (compared to the MLP-based model from the previous chapter). In the sequel, we refer to this alternative as the "equation-based model".

The thermodynamic origin of (4.1) is the Nernst equation [41] that expresses the interfacial ionic equilibrium potential E as follows:

$$E = E^0 + \frac{RT}{\nu F} \ln \frac{c_1}{c_2}, \tag{4.2}$$

where E^0 is the so-called formal potential, R is the gas constant, F is the Faraday constant, and ν is the ion charge, while c_1 and c_2 are ion concentrations at the two sides of the interface. Equation (4.1) mimics the structure of the above Nernst equation with $V_{OC} = E$, $V_o = E^0$, $\varphi = RT/(\nu F)$, $c_1 = \alpha_p - C(t)$, and $c_2 = \alpha_n + C(t)$.

4.2 Training Details

4.2.1 Initialization of Trainable Parameters

Among the trainable parameters of the OCV equation given by (4.1), V_o has been initialized to 0.5 prior to training. Meanwhile, φ has been initialized to 0.1, with an additional constraint that this parameter must always be non-negative. On the other hand, α_n and α_p have been initialized randomly within specific ranges [0.1, 1.0] and [1.1, 2.0], respectively. The summary of the initialization is given in Table 4.1.

Table 4.1: Parameter Initialization for OCV Equation

Parameters	**Constraint**	**Initial Value**
V_o	N/A	0.5
φ	Non-negative	0.1
α_n	N/A	Random(0.1 to 1.0)
α_p	N/A	Random(1.1 to 2.0)

4.2.2 Training Process

The training setup was the same as described in the previous chapter, using the same training and validation datasets. The training time was 1 hour and 4 minutes (i.e., very similar to the time reported in Chapter 3), which is dominated by the optimization of over 2K parameters of the LSTM in Wing B. The training loss curve is shown in Figure 4.1. The smallest validation error has been found at the 28th epoch, where the training MAE and Validation MAE were 0.018 and 0.067, respectively. These values are practically the same as those reported for the MLP-based model (0.018 and 0.066, respectively). It illustrates that the MLP with 105 parameters was effectively replaced by the explainable OCV equation with only 4 parameters. Their optimized values are listed in Table 4.1.

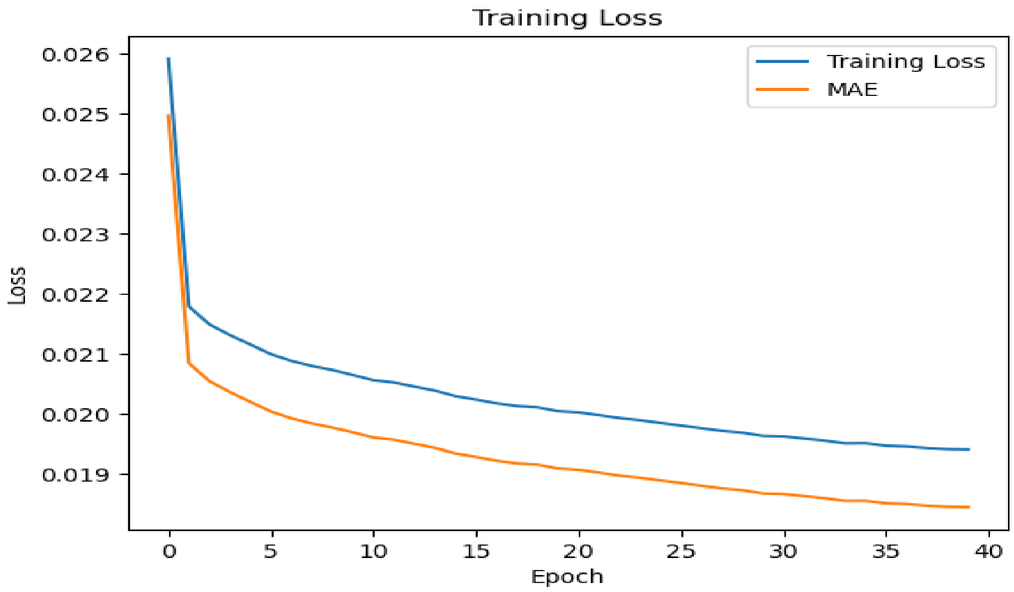

Figure 4.1: Custom Training Loss vs Mean Absolute Error

Table 4.2: Optimized Parameters of OCV Equation

Parameters	**Optimized Value**
V_o	0.66
φ	0.61
α_n	1.32
α_p	2.2

4.3 Test Result

The testing process was identical to the one described in Chapter 3. The overall test results are summarized in Table 4.3 and depicted in Figure 4.2. The predicted voltage and the ground truth are plotted in Figures 4.3, 4.5, 4.7, and 4.9 (along with the errors curves). The corresponding plots of the V_{OC} and ΔV predictions are shown in Figures 4.4, 4.6, 4.8, and 4.10.

Table 4.3: Summary of Test Results for Equation-Based Model

Ambient Temp.	**MAPE (%)**	**RMSPE (%)**	**Worst Case Overestimation (V)**	**Worst Case Underestimation (V)**
-10 °C	0.76	1.42	0.48	0.26
0 °C	0.64	1.10	0.37	0.17
10 °C	0.70	1.18	0.30	0.12
25 °C	0.72	1.22	0.30	0.09

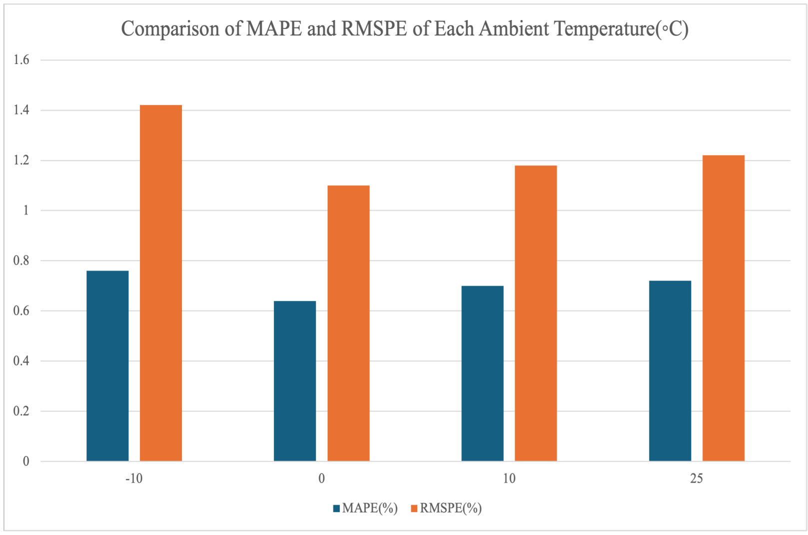

Figure 4.2: MAPE and RMSPE of Equation-Based Model

The MAPE is 0.76% at -10 °C, which drops to 0.64% at 0 °C. It marginally increases to 0.70% at 10 °C, and then to 0.72% at 25 °C. Similarly to the MAPE, the largest RMSPE of 1.42% occurs at -10 °C. The RMSPE drops to 1.1% at 0 °C and then rises to 1.18% at 10 °C and to 1.22% at 25 °C.

With the lowest MAPE (0.64%) and RMSPE (1.1%), the model performs best at 0 °C. The model performs worst at -10 °C, with the slightly larger RMSPE (1.42%) and MAPE (0.76%). It should be mentioned that the largest MAPE (0.76%) of the equation-based model is slightly better than that of the MLP-based model from Chapter 3 (0.82%). However, the largest RMSPE (1.42%) of the equation-based model is slightly worse than that of the MLP-based model (1.28%).

The worst-case overestimation of 0.48 V occurs at -10 °C, which decreases to 0.37 V at 0 °C and then to 0.30 V at 10 °C and 25 °C. These occurrences are depicted in Figure 4.11, where one can observe the presence of a dynamic bias (as in Figure 3.12 for the MLP-based model).

The worst-case underestimation happens at -10 °C (0.26 V), which drops to 0.17 V at 0 °C and then to 0.12 V at 10 °C. At 25 °C, we have the smallest worst-case underestimation of only 0.09 V. This implies that the model gets more accurate as the temperature rises. Recall that the same trend was observed for the MLP-based model as well.

Finally, it is worth highlighting that the first wing output of the equation-based model also looks similar to the first wing output of the MLP-based model. This

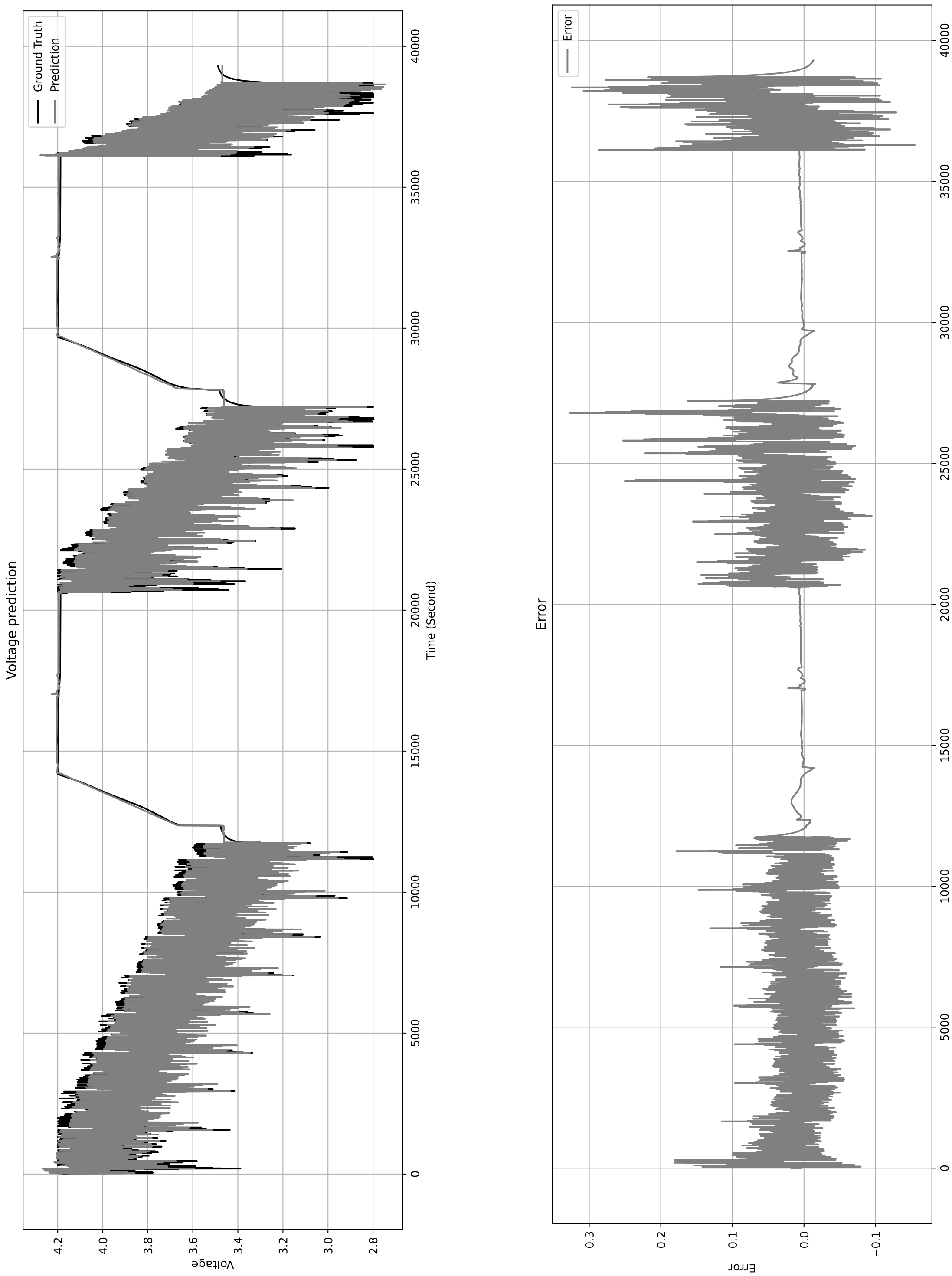

(a) Predicted Voltage vs Ground Truth

(b) Error (Predicted Voltage - Ground Truth)

Figure 4.3: Equation-Based Model, Test Results at -10 °C

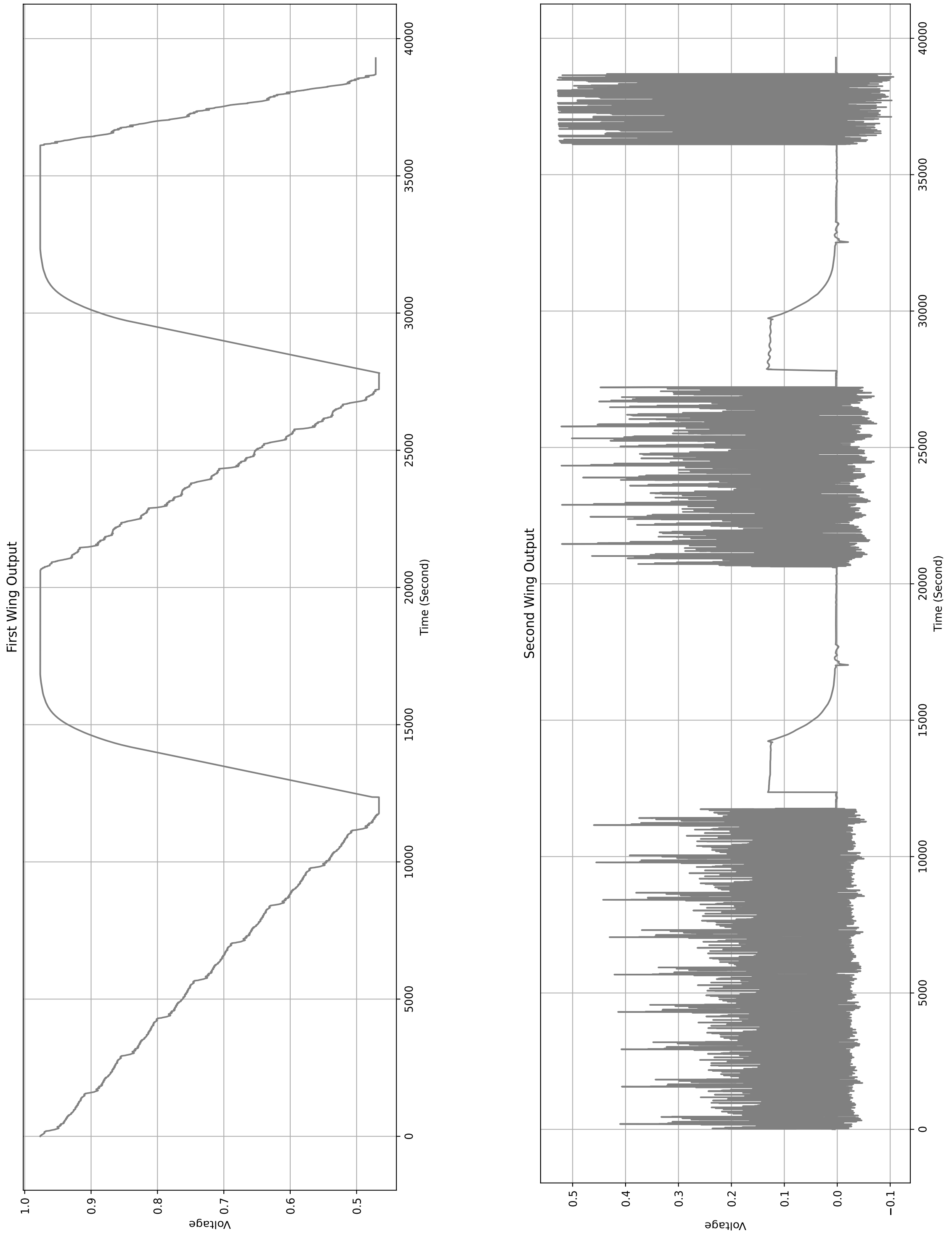

(a) First Wing Output

(b) Second Wing Output

Figure 4.4: Individual Wing Outputs of Equation-Based Model, -10 °C Data.

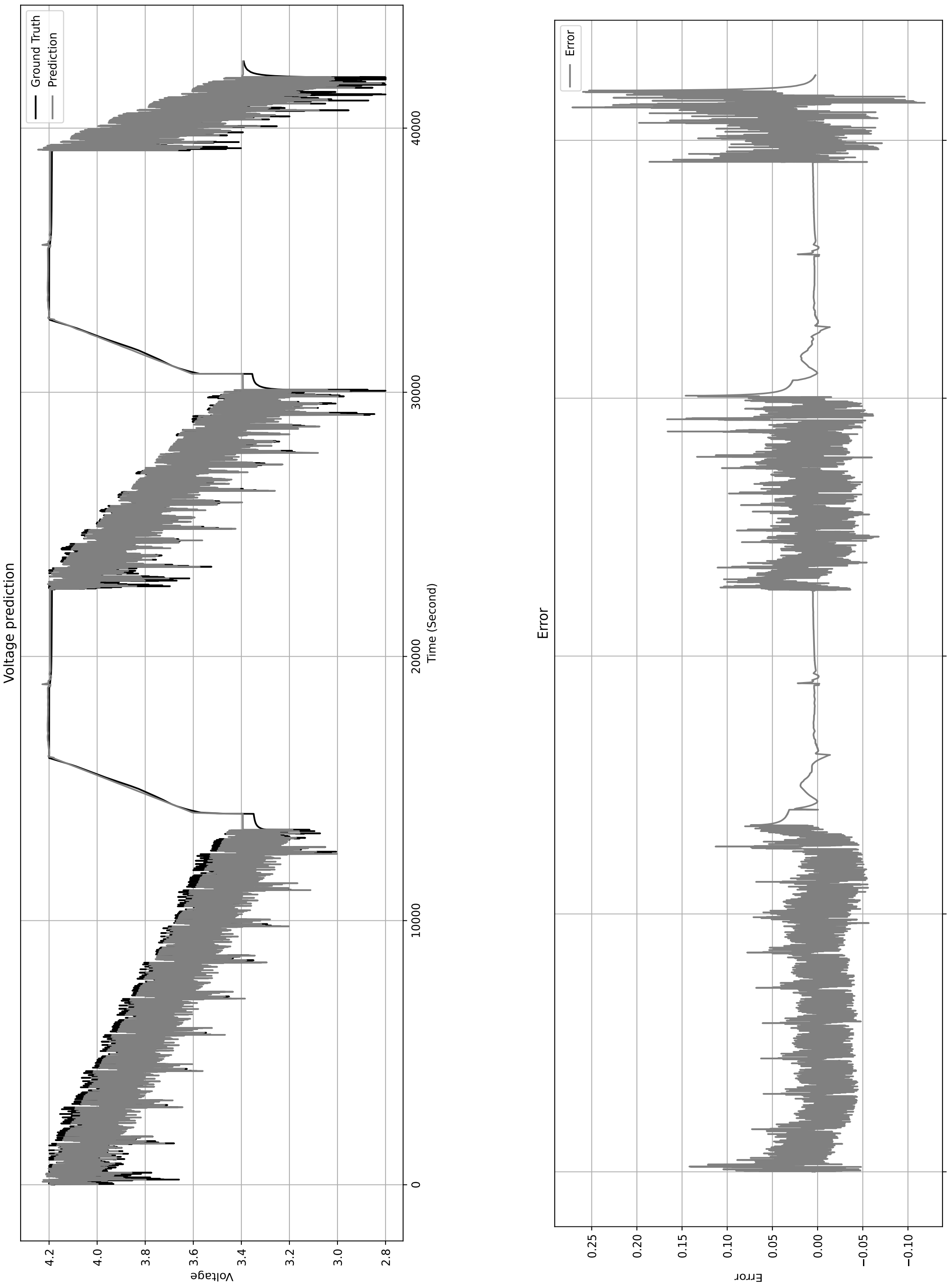

(a) Predicted Voltage vs Ground Truth (b) Error (Predicted Voltage - Ground Truth)

Figure 4.5: Equation-Based Model, Test Results at 0°C

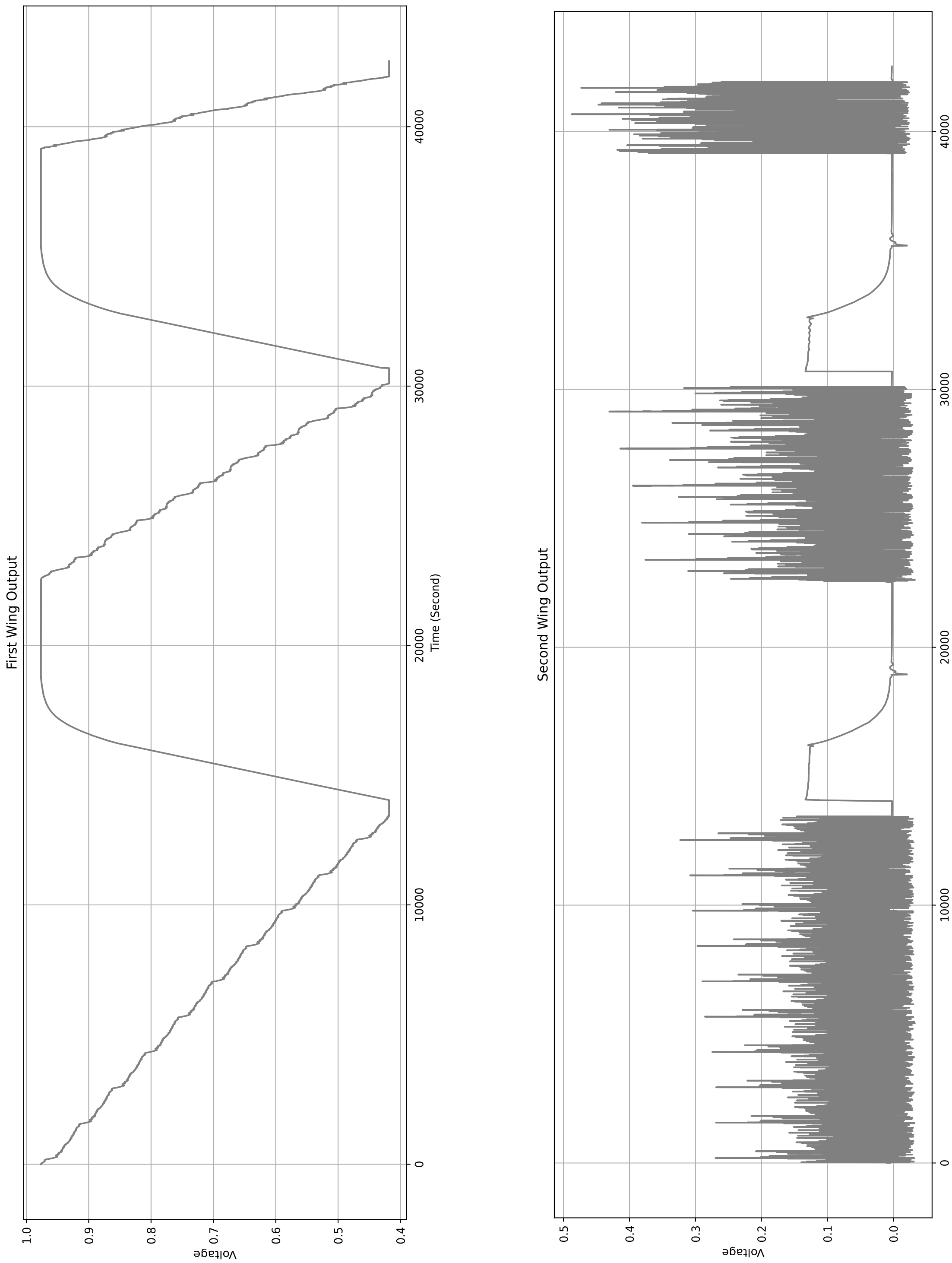

(a) First Wing Output

(b) Second Wing Output

Figure 4.6: Individual Wing Outputs of Equation-Based Model, 0 °C Data.

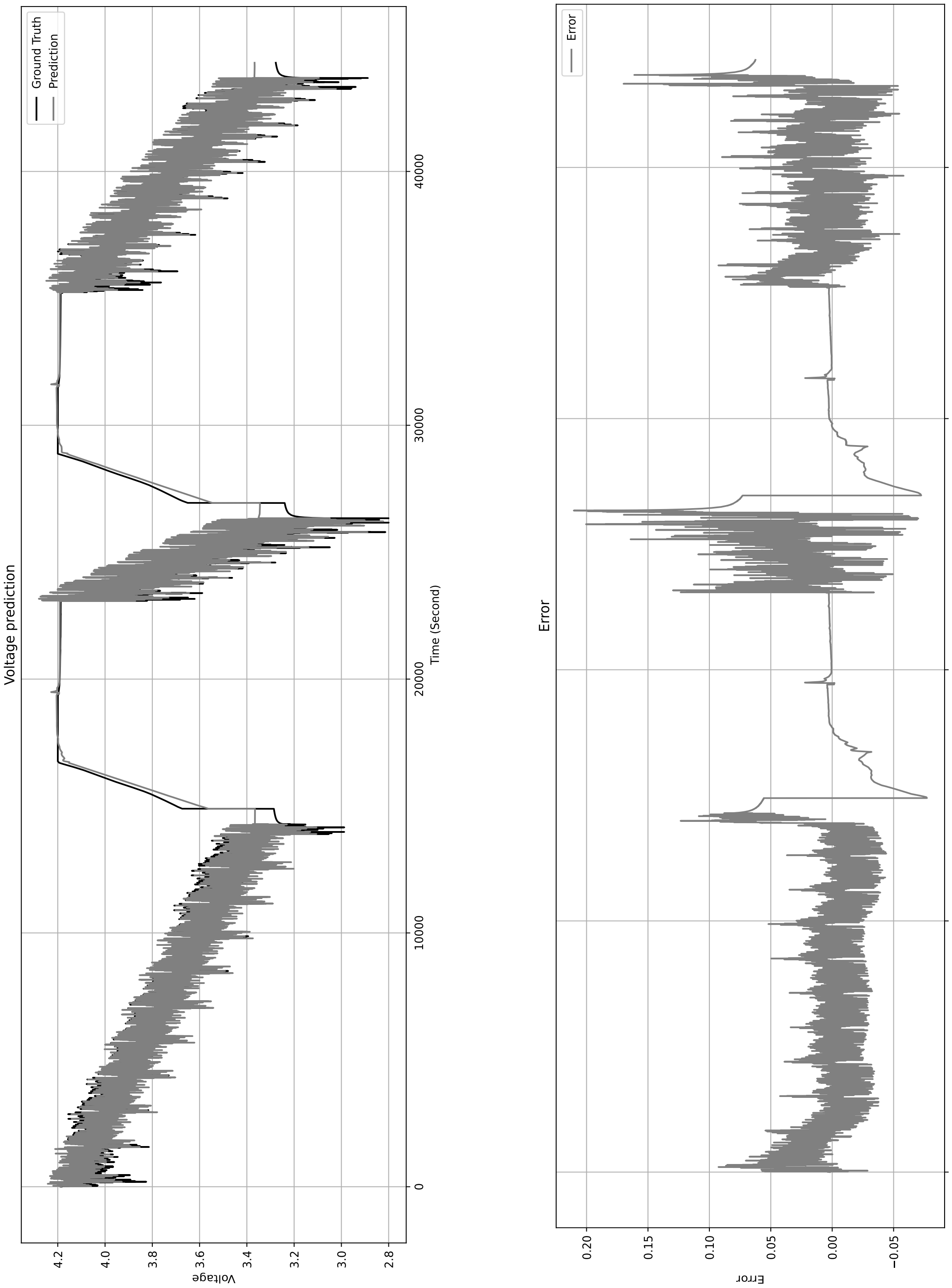

(a) Predicted Voltage vs Ground Truth

(b) Error (Predicted Voltage - Ground Truth)

Figure 4.7: Equation-Based Model, Test Results at 10 °C

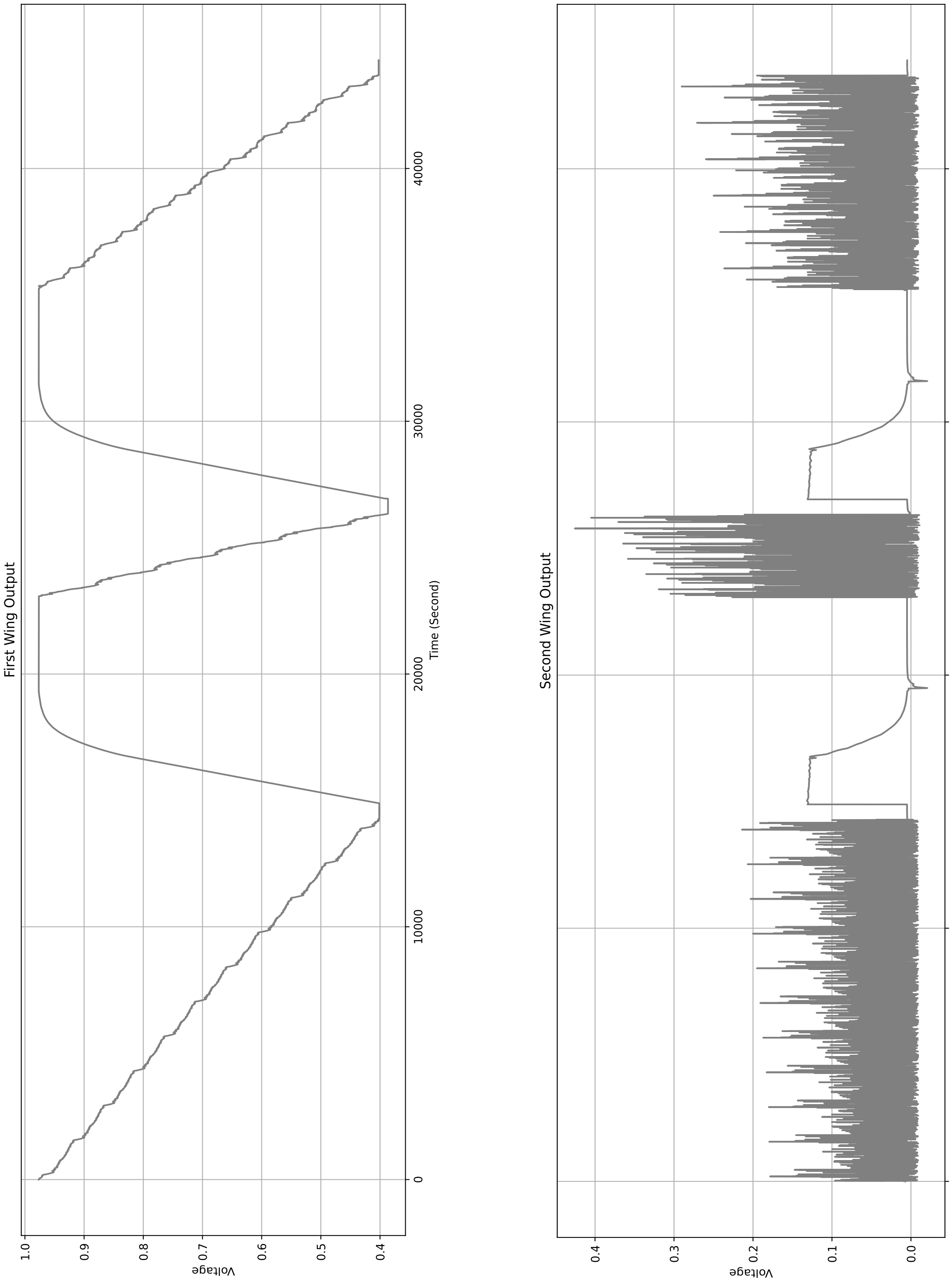

(a) First Wing Output

(b) Second Wing Output

Figure 4.8: Individual Wing Outputs of Equation-Based Model, 10 °C Data.

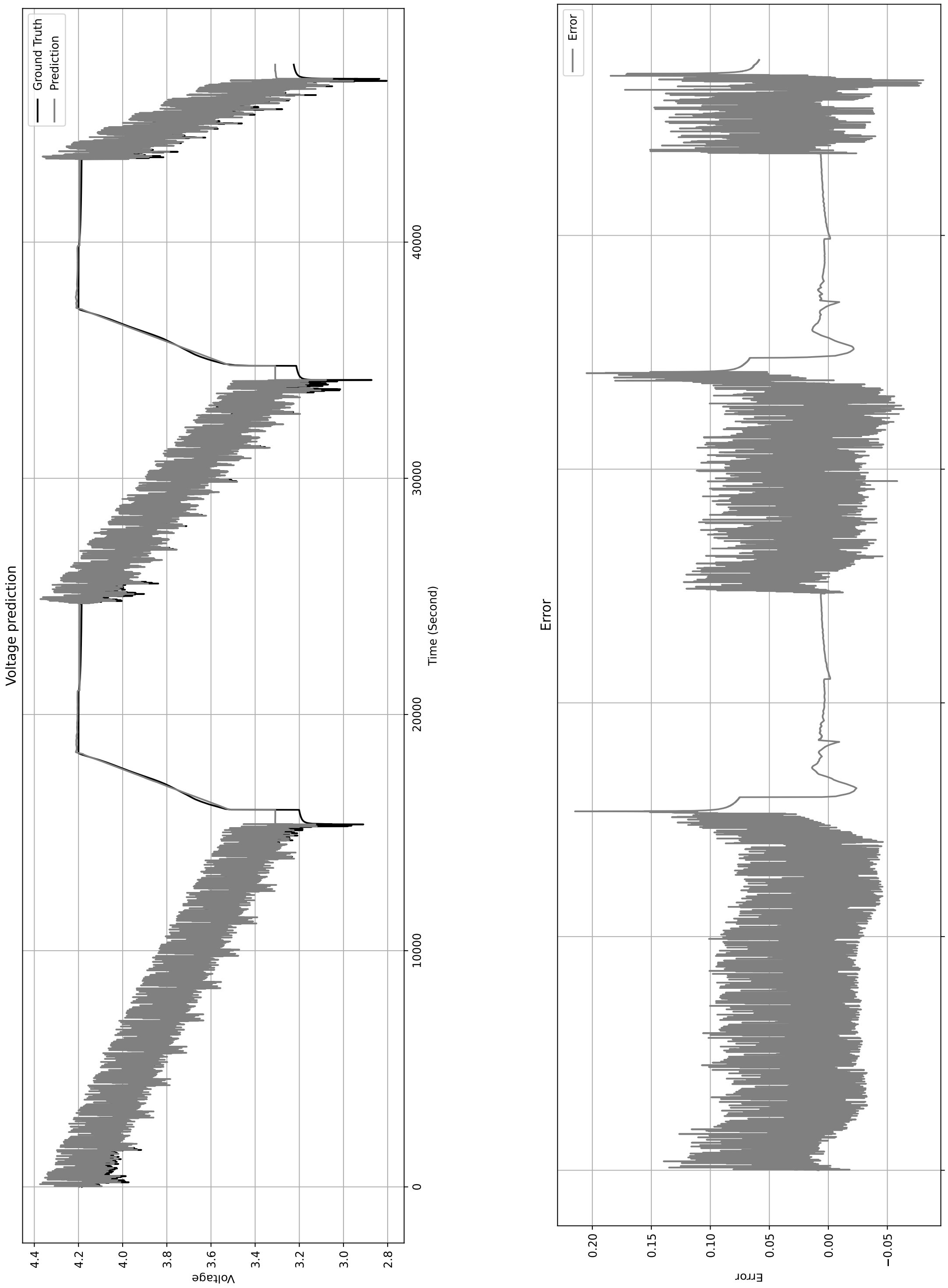

(a) Predicted Voltage vs Ground Truth

(b) Error (Predicted Voltage - Ground Truth)

Figure 4.9: Equation-Based Model, Test Results at 25 °C

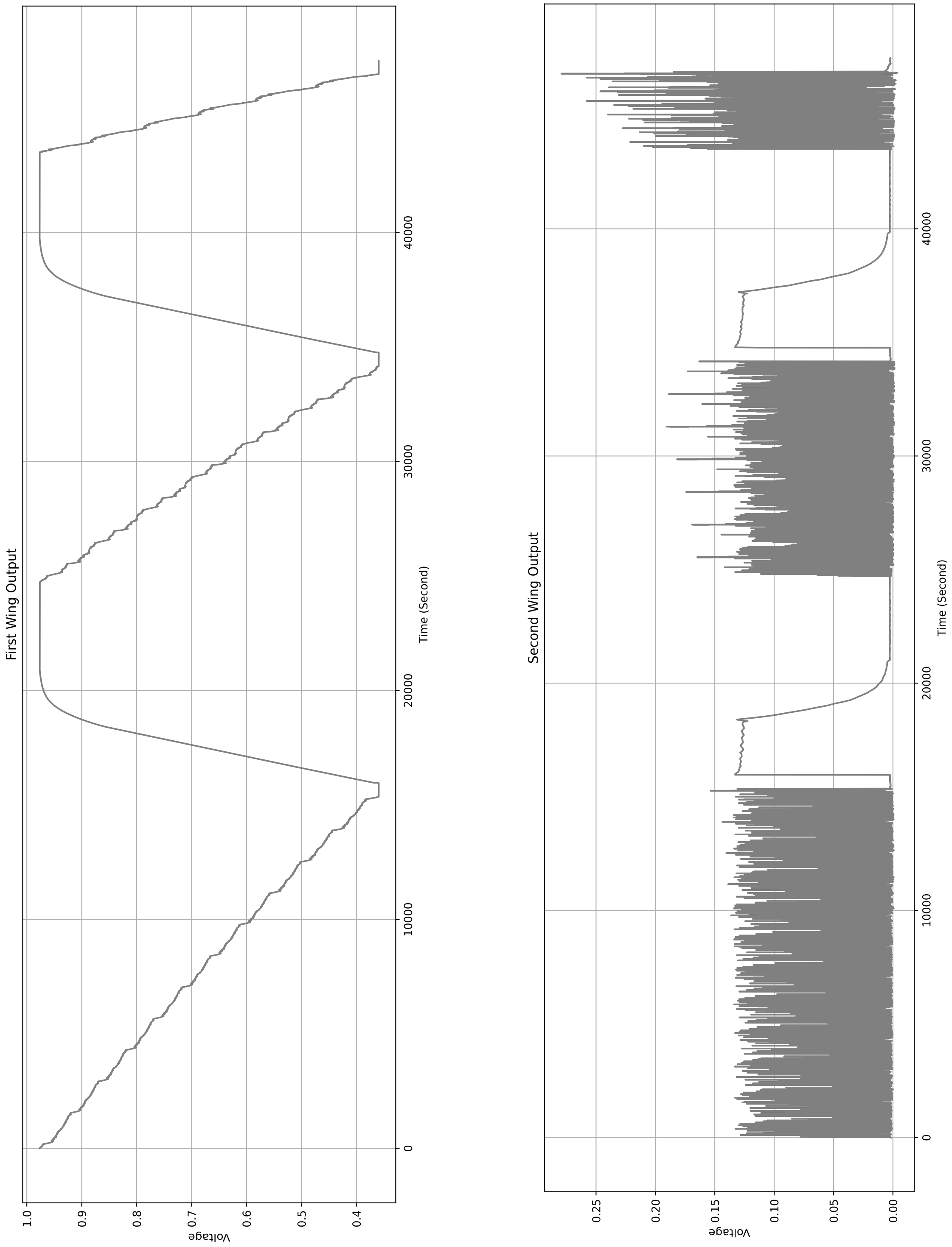

(a) First Wing Output

(b) Second Wing Output

Figure 4.10: Individual Wing Outputs of Equation-Based Model, 25 °C Data.

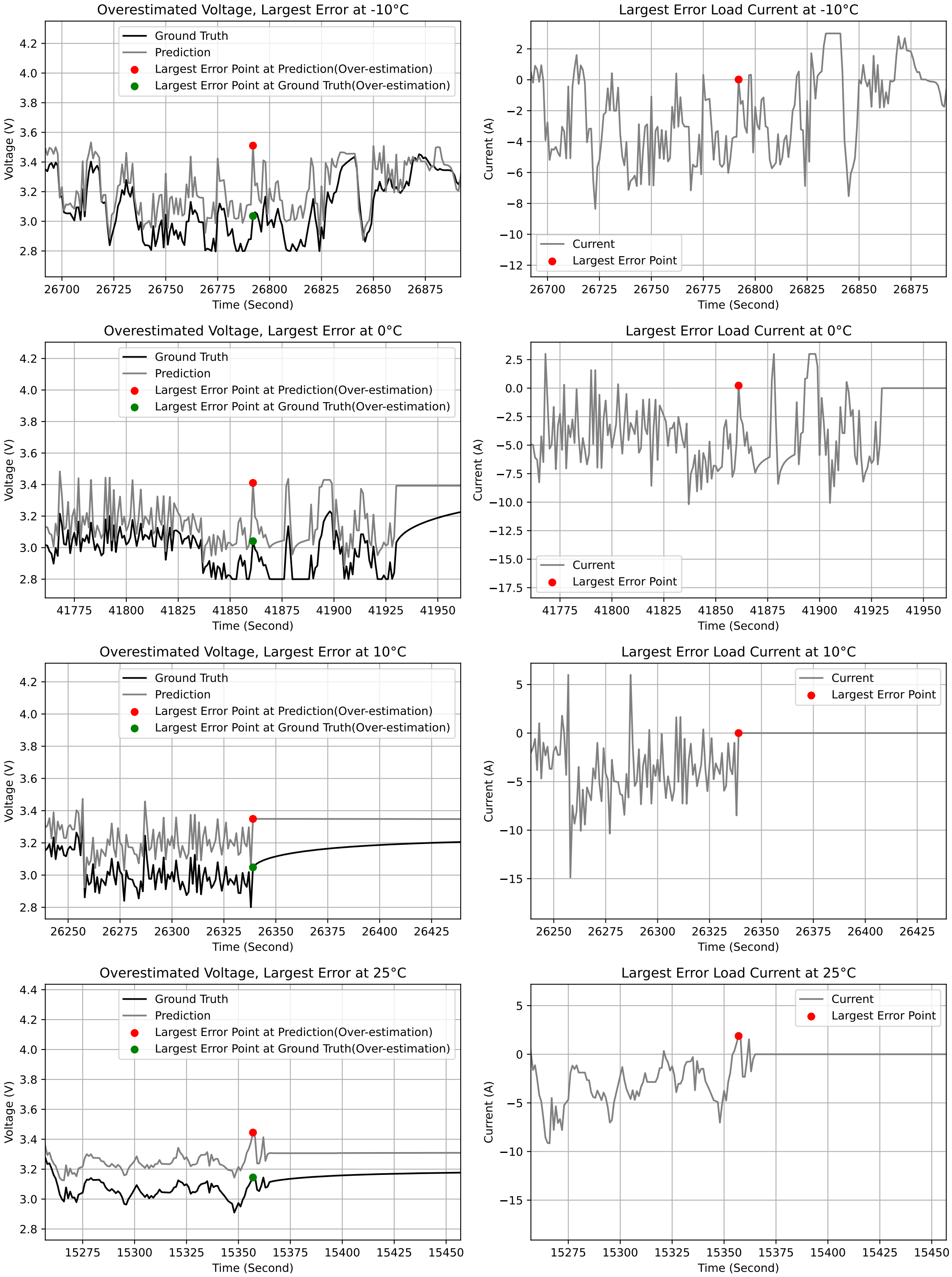

Figure 4.11: Worst-Case Voltage Overestimation by Equation-Based Model

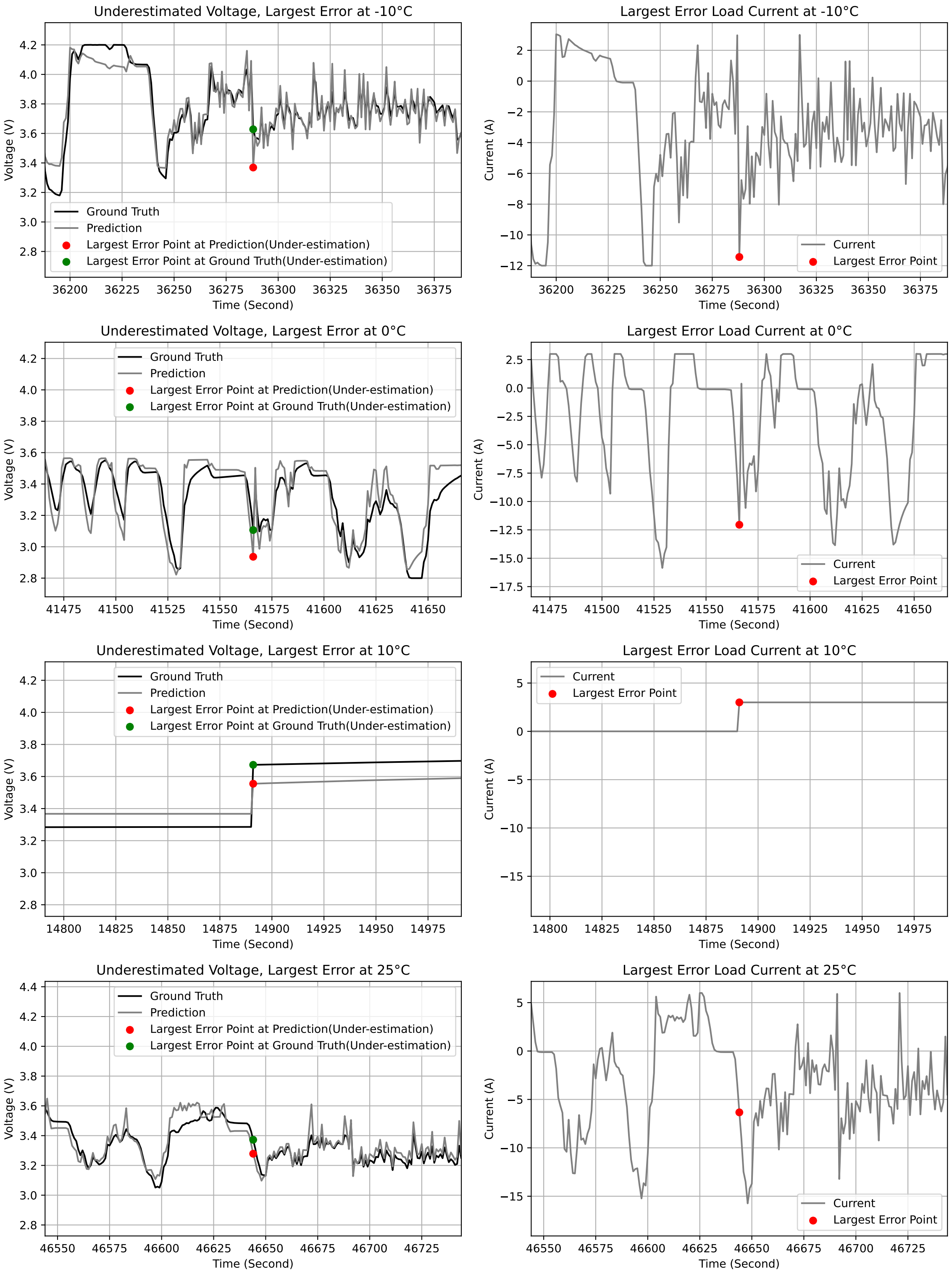

Underestimated Voltage, Largest Error at -10°C

Largest Error Load Current at -10°C

Underestimated Voltage, Largest Error at 0°C

Largest Error Load Current at 0°C

Underestimated Voltage, Largest Error at 10°C

Largest Error Load Current at 10°C

Underestimated Voltage, Largest Error at 25°C

Largest Error Load Current at 25°C

Figure 4.12: Worst-Case Voltage Underestimation by Equation-Based Model

evidence further demonstrates that the equation-based can successfully compete with the MLP-based OCV predictor. However, the former is more efficient as it requires less memory and involves fewer computations.

Chapter 5

Comparison of MLP-Based and Equation-Based Models

5.1 Structural Difference

Deep neural networks (DNNs) are often referred to as universal approximators due to their ability to model complex relationships within data [42]. An MLP has been used in this study in Chapter 3 as a DNN example for modeling the OCV behavior. It consists of multiple layers of interconnected neurons, each capable of processing input information by applying local weights and biases. To introduce non-linearity, activation functions like ReLU are applied in the hidden layers. However, one of the significant drawbacks of DNNs is their "black box" nature, making the prediction process difficult to interpret.

In contrast, Chapter 4 utilizes an approximate equation from [8] as the OCV predictor. It has been derived mathematically and offers a transparent and explainable tool for understanding the OCV behaviour. This equation is non-linear, and it requires only four parameters, making it computationally efficient for this specific task.

Despite its advantages, the OCV equation does not account for the influence of temperature. Conversely, any MLP can incorporate temperature as another input and capture its influence after training. However, to make the equation-based OCV predictor directly comparable to its MLP counterpart, temperature $T(t)$ was not taken as the input of the MLP model.

5.2 Performance Difference

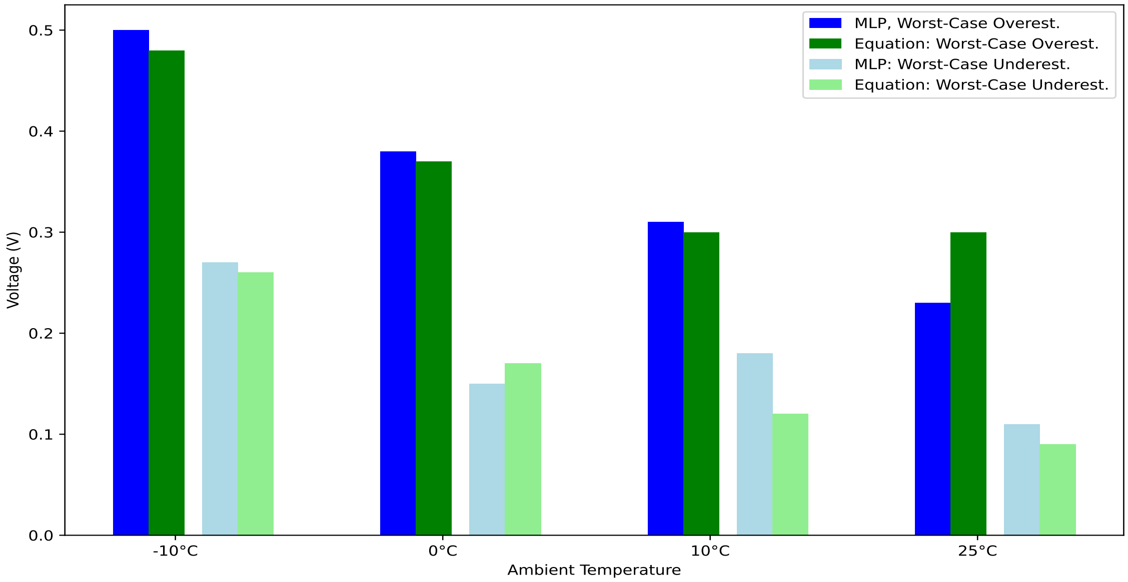

Figure 5.1: Comparison of Worst-Case Voltage Overestimation and Underestimation Errors

Table 3.3 and Table 4.3 in the previous chapters illustrate the performance of the MLP-based and equation-based models, using such indicators as the MAPE, RMSPE, worst-case overestimation, and worst-case underestimation. The corresponding bar charts are shown in Figures 5.1 and 5.2. At -10 °C, the MLP-based model overestimated the battery voltage by 0.50 V in the worst case, which is slightly higher than the equation-based model's error of 0.48 V. As the temperature increases, the worst-case overestimation error of the MLP-based model drops to 0.38 V at 0 °C, 0.31 V at 10 °C, and 0.23 V at 25 °C. The equation-based model shows a similar trend, producing the worst-case overestimates of 0.37 V at 0 °C and 0.30 V at 10 °C and 25 °C. Note that the voltage-based model outperforms the MLP-based model in all cases but one (specifically, at 25 °C).

As for the worst-case underestimation errors, the MLP-based model gives 0.27 V at -10 °C, 0.15 V at 0 °C, 0.18 V at 10 °C, and 0.11 V at 25 °C. Meanwhile, the equation-based model's errors are 0.26 V at -10 °C, 0.17 V at 0 °C, 0.12 V at 10 °C, and 0.09 V at 25 °C. Note that the equation-based model outperforms the MLP-based model in all cases but one (specifically, at 0 °C).

When we compare the MAPE and RMSPE at -10 °C and 25 °C (see Figure 5.2),

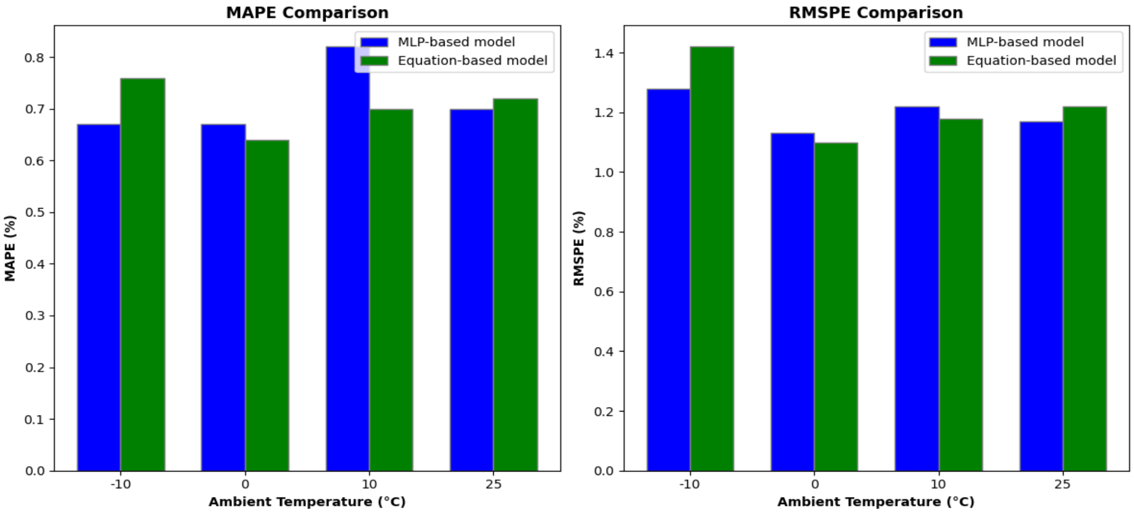

Figure 5.2: Comparison of MAPE and RMSPE

the MLP-based model performs better than the equation-based model, producing smaller MAPE (0.67% vs. 0.76% at -10 °C and 0.70% vs. 0.72% at 25 °C) and smaller RMSPE (1.28% vs. 1.42% at -10 °C and 1.17% vs. 1.22% at 25 °C). On the other hand, at 0 °C and 10°C, the equation-based model performs better than the MLP-based model, producing smaller MAPE (0.64% vs. 0.67% at 0 °C and 0.70% vs. 0.82% at 10 °C) and smaller RMSPE (1.10% vs. 1.13% at 0 °C and 1.18% vs. 1.22% at 10 °C). Overall, it should be noted that the error differences mentioned above are relatively small. This indicates that both models are competitive with each other in terms of their prediction accuracy.

Figure 5.3 further illustrates the similarity between the MLP and equation-based models. It shows their predicted voltage curves at -10 °C within some selected time window. Recall that both models produced the largest worst-case overestimation error at this temperature and within this time window (see Figures 3.12 and 4.11). As one can see in Figure 5.3, the voltage predictions given by the two models are very close.

In Figure 5.3, it appears that the equation-based model is generating slightly lower voltage values compared to the MLP-based model. Since our modeling approach allows us to break down such predictions into the V_{OC} and ΔV components, Figure 5.4 shows each model's OCV prediction curves to illustrate the difference between the MLP and equation outputs. These curves demonstrate that most of the time, the OCV equation produces slightly smaller values compared to the MLP. However, at

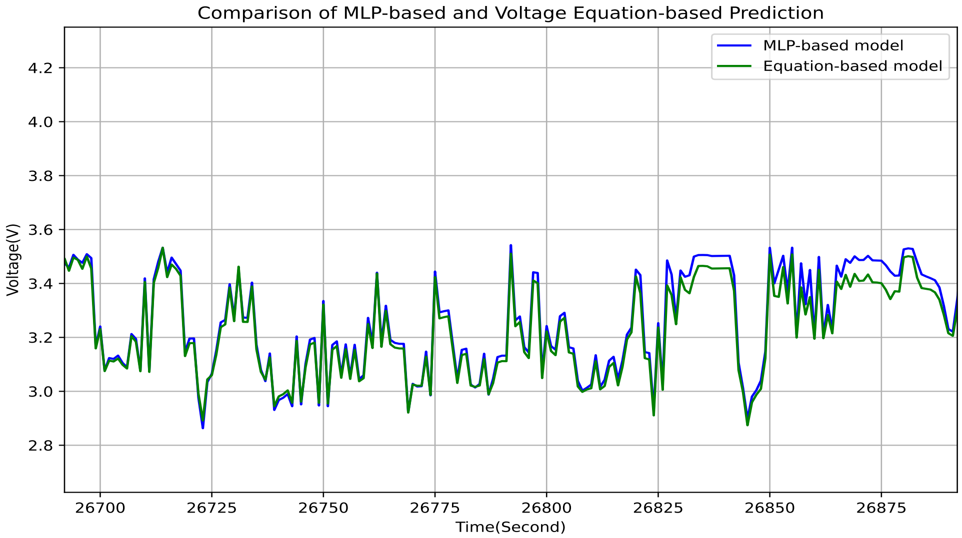

Figure 5.3: Comparison of Predicted voltage generated by MLP and Voltage Equation-based Model at -10 °C

10 °C and 25 °C, the OCV equation's predicted values are higher than those of the MLP. Since the utilized test dataset does not contain the ground truth for the OCV, it is difficult to determine which OCV predictor is more accurate in our case.

5.3 Comparison to Related Work

The closest related work on DL-based EV battery voltage modeling is due to Liang *et al.* [17]. Unfortunately, the dataset utilized in [17] is different from the one used here. The experimental measurements (not publicly available) were performed on a different battery, which prevents direct comparisons. Nevertheless, for the sake of completeness, we describe key details of their work below and compare it to ours indirectly.

A 47-Ah pouch cell (with NMC/graphite chemistry) from a Chrysler Pacifica Hybrid vehicle was used in [17]. Its nominal operating voltage was 3.65 V, while the minimum and maximum voltage limits were 2.7 and 4.25 V, respectively. In our case, the measurement data were acquired on a 3-Ah LG Li-ion cell, where the nominal voltage was 3.6 V, and the minimum and maximum voltage limits were 2.79 and 4.23 V, respectively. Four drive cycles (US06, LA92, HWFET, and UDDS) were utilized for testing a DL model that predicted the terminal voltage as a whole. In our case,

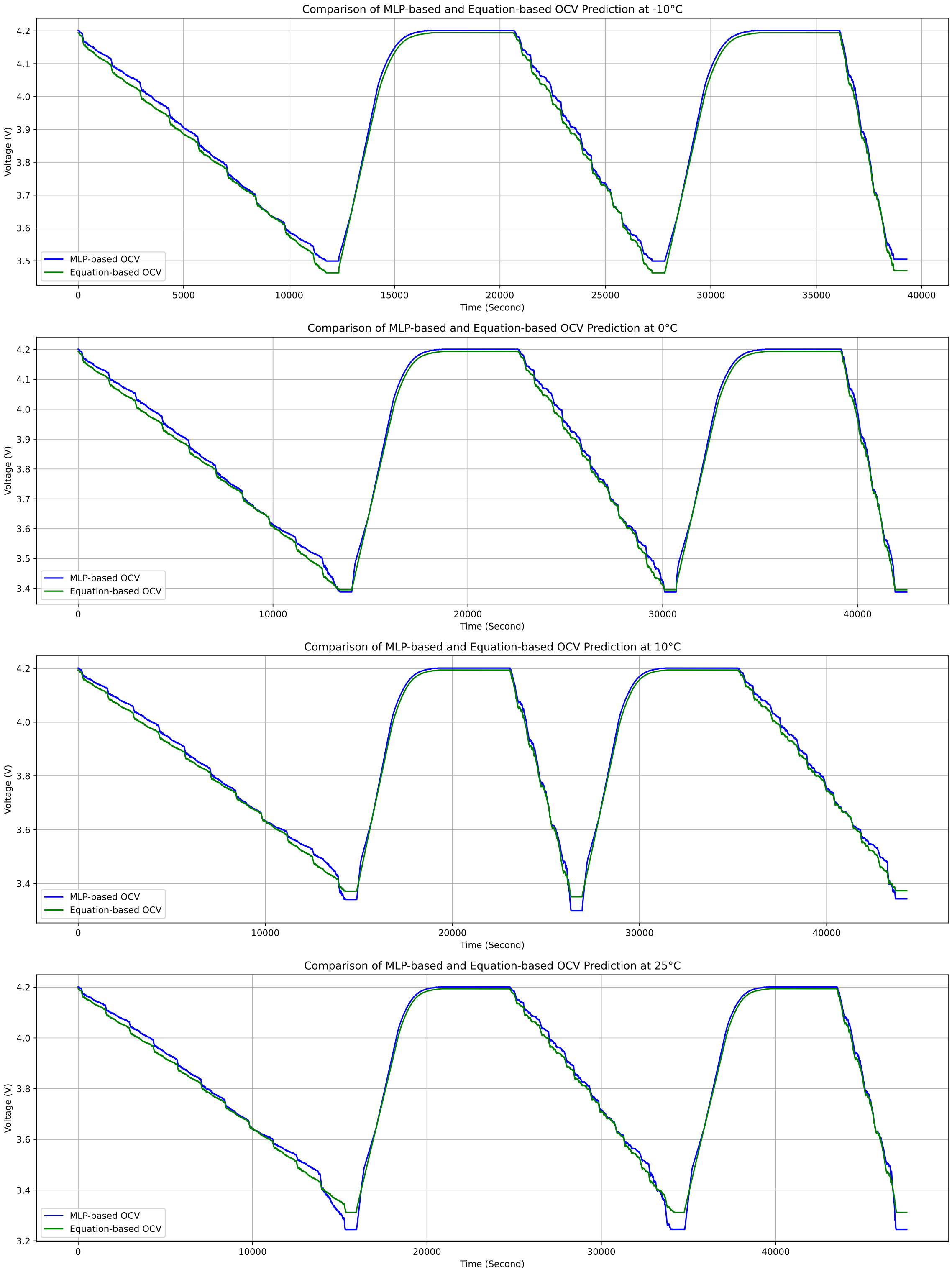

Figure 5.4: MLP-Based and Equation-Based Model Predictions of OCV

the test data were comprised of three drive cycles (US06, LA92, and UDDS), while the evaluated models were predicting the terminal voltage as a separable combination of V_{OC} and ΔV. Liang *et al.* used an LSTM-based model with ten cells followed by a fully connected layer coupled with the clipped ReLU activation function. This model achieved RMSE values ranging from 9 to 60 mV across four temperatures (-10 °C, 0 °C, 10 °C, and 25 °C) for UDDS, LA92, and US06.

In our case, the RMSE for both the MLP- and equation-based models ranged from 32 to 112 mV across all three drive cycles and all four temperatures under consideration. It is worth reiterating that these numbers correspond to the measurements taken on a different EV battery, i.e., they are not directly comparable to those from [17]. Our models require under 2.6K parameters in total, which is considered lightweight (in comparison to typical deep learning networks having millions of parameters). As mentioned earlier, this parameter count is mainly due to the presence of 16 LSTM cells (preceded by a convolutional layer) inside the ΔV predictor. In contrast, the model from [17] was reported to have about 800 parameters, i.e., it is lighter. However, the key advantage of our models is their enhanced explainability.

Chapter 6

Conclusions

Lithium-ion (Li-ion) batteries play a critical role in diverse applications, including renewable energy storage, portable electronics, and EVs [43]. To facilitate efficient and sustainable operation, a BMS is essential. The BMS monitors and manages various parameters of the battery, such as the SoC, SoH, state of energy (SoE), and terminal voltage [44]. Among these, accurate voltage predictions in relation to the load current can be highly valuable. Since a battery must operate within certain maximum and minimum voltage limits, early and accurate voltage estimation can enable better control over the battery load, optimizing the discharge and recharge cycles and thus extending battery lifetime. In other words, battery voltage prediction can play an important role in preventing issues such as overcharging and over-discharging, both of which can compromise battery safety and performance.

DL models have been shown to improve the BMS performance, as they are capable of discovering and exploiting hidden patterns in the battery data. Such models are typically treated as black boxes, because it is usually difficult to explain their behavior. The primary goal of this study is to make the DL-based voltage prediction process more explainable without compromising the accuracy.

We have proposed a novel two-wing architecture. The first wing takes the consumed charge $C(t)$ over time t (obtained via Coulomb counting) and predicts the steady-state OCV component $V_{OC}(t)$. The second wing takes the instantaneous current $I(t)$ and the cell temperature $T(t)$, and it predicts the transient voltage component $\Delta V(t)$. The OCV and transient components are then combined into the terminal voltage prediction $V(t)$ using a single-layer perceptron.

An LSTM-based structure was used in the second wing (i.e., the ΔV predictor) to capture the discharge/charge current history, which is important for the determination of the voltage change. On the other hand, the first wing (i.e., the OCV predictor) was designed using two different approaches. The first approach used an MLP structure with 105 learnable parameters, while the second approach used an approximate 4-parameter OCV equation from [8]. A well-known experimental dataset from [21] was used for training, validation, and testing purposes. This dataset represents measurements taken on an LG 18650HG2 Li-ion battery cell subjected to typical loads associated with EV drive cycles (combined with charge cycles) at various ambient temperatures. In this study, the considered temperatures were -10 °C, 0 °C, 10 °C, and 25 °C.

The MLP-based model estimated the battery voltage with the MAPE range from 0.67% to 0.82%. The equation-based model estimated voltage the battery voltage with the MAPE range from 0.64% to 0.76%. The worst-case scenario of overestimation and underestimation was observed at -10°C for both approaches. The predicted voltage was overestimated by 0.50V by the MLP-based model and 0.48V by the voltage equation-based model. While such errors are relatively large, they correspond to the worst case only, i.e., not the overall average across the entire test dataset.

Future work could focus on developing a more accurate OCV equation that can take temperature as an input, in addition to the consumed charge. Alternatively, the OCV-predicting MLP can be supplied with the temperature information and be trained accordingly. Another interesting direction would be to explore reinforcement learning in the BMS context [45]. The basic idea is to check the past predictions of a voltage model with the measured values during the battery operation and then use detected differences to recalibrate the model parameters dynamically. This can be used, for example, as a mechanism for implementing a self-correcting dynamic bias briefly mentioned at the end of Chapter 3. Finally, one should investigate the effect of battery aging on voltage predictions, as our current modeling approach does not account for it, mainly due to the lack of training data.

Bibliography

[1] M. H. Lipu, M. Hannan, T. F. Karim, A. Hussain, M. H. M. Saad, A. Ayob, M. S. Miah, and T. I. Mahlia, “Intelligent algorithms and control strategies for battery management system in electric vehicles: Progress, challenges and future outlook,” *Journal of Cleaner Production*, vol. 292, p. 126044, 2021.

[2] E. E. Agency, “Greenhouse gas emissions from transport in europe.” https://www.eea.europa.eu/en/analysis/indicators/greenhouse-gas-emissions-from-transport. Accessed: 2024-12-15.

[3] I. B. Espedal, A. Jinasena, O. S. Burheim, and J. J. Lamb, “Current trends for state-of-charge (SoC) estimation in lithium-ion battery electric vehicles,” *Energies*, vol. 14, no. 11, p. 3284, 2021.

[4] L. H. Saw, Y. Ye, and A. A. Tay, “Integration issues of lithium-ion battery into electric vehicles battery pack,” *Journal of Cleaner Production*, vol. 113, pp. 1032–1045, 2016.

[5] K. Okay, S. Eray, and A. Eray, “Development of prototype battery management system for PV system,” *Renewable Energy*, vol. 181, pp. 1294–1304, 2022.

[6] M. K. Hasan, M. Mahmud, A. A. Habib, S. Motakabber, and S. Islam, “Review of electric vehicle energy storage and management system: Standards, issues, and challenges,” *Journal of Energy Storage*, vol. 41, p. 102940, 2021.

[7] K. Li, F. Wei, K. J. Tseng, and B.-H. Soong, “A practical lithium-ion battery model for state of energy and voltage responses prediction incorporating temperature and ageing effects,” *IEEE Transactions on Industrial Electronics*, vol. 65, no. 8, pp. 6696–6708, 2017.

[8] D. Rakhmatov, "Battery voltage modeling for portable systems," *ACM Transactions on Design Automation of Electronic Systems (TODAES)*, vol. 14, no. 2, pp. 1–36, 2009.

[9] M. Naguib, P. Kollmeyer, and A. Emadi, "Lithium-ion battery pack robust state of charge estimation, cell inconsistency, and balancing," *IEEE Access*, vol. 9, pp. 50570–50582, 2021.

[10] D. Theuerkauf and L. Swan, "Characteristics of open circuit voltage relaxation in lithium-ion batteries for the purpose of state of charge and state of health analysis," *Batteries*, vol. 8, no. 8, p. 77, 2022.

[11] J. Tian, R. Xiong, W. Shen, and J. Lu, "State-of-charge estimation of lifepo4 batteries in electric vehicles: A deep-learning enabled approach," *Applied Energy*, vol. 291, p. 116812, 2021.

[12] K. Kaur, A. Garg, X. Cui, S. Singh, and B. K. Panigrahi, "Deep learning networks for capacity estimation for monitoring SOH of li-ion batteries for electric vehicles," *International Journal of Energy Research*, vol. 45, no. 2, pp. 3113–3128, 2021.

[13] D. N. How, M. A. Hannan, M. S. H. Lipu, K. S. Sahari, P. J. Ker, and K. M. Muttaqi, "State-of-charge estimation of li-ion battery in electric vehicles: A deep neural network approach," *IEEE Transactions on Industry Applications*, vol. 56, no. 5, pp. 5565–5574, 2020.

[14] Y. Feng and Z. Dong, "Optimal energy management with balanced fuel economy and battery life for large hybrid electric mining truck," *Journal of Power Sources*, vol. 454, p. 227948, 2020.

[15] S. Wang, P. Takyi-Aninakwa, S. Jin, C. Yu, C. Fernandez, and D.-I. Stroe, "An improved feedforward-long short-term memory modeling method for the whole-life-cycle state of charge prediction of lithium-ion batteries considering current-voltage-temperature variation," *Energy*, vol. 254, p. 124224, 2022.

[16] Y. Gao, C. Zhu, X. Zhang, and B. Guo, "Implementation and evaluation of a practical electrochemical-thermal model of lithium-ion batteries for ev battery management system," *Energy*, vol. 221, p. 119688, 2021.

[17] Y. Liang, A. Emadi, O. Gross, C. Vidal, M. Canova, S. Panchal, P. Kollmeyer, M. Naguib, and F. Khanum, "A comparative study between physics, electrical and data driven lithium-ion battery voltage modeling approaches," tech. rep., SAE Technical Paper, 2022.

[18] S. M. Shahriar, E. A. Bhuiyan, M. Nahiduzzaman, M. Ahsan, and J. Haider, "State of charge estimation for electric vehicle battery management systems using the hybrid recurrent learning approach with explainable artificial intelligence," *Energies*, vol. 15, no. 21, p. 8003, 2022.

[19] J. Zhu, Y. Wang, Y. Huang, R. Bhushan Gopaluni, Y. Cao, M. Heere, M. J. Mühlbauer, L. Mereacre, H. Dai, X. Liu, *et al.*, "Data-driven capacity estimation of commercial lithium-ion batteries from voltage relaxation," *Nature Communications*, vol. 13, no. 1, p. 2261, 2022.

[20] Q. Zhang, N. Cui, Y. Li, B. Duan, and C. Zhang, "Fractional calculus based modeling of open circuit voltage of lithium-ion batteries for electric vehicles," *Journal of Energy Storage*, vol. 27, p. 100945, 2020.

[21] P. Kollmeyer, C. Vidal, M. Naguib, and M. Skells, "Lg 18650hg2 li-ion battery data and example deep neural network xEV soc estimator script," *Mendeley Data*, vol. 3, p. 2020, 2020.

[22] M. M. Maricq, J. J. Szente, A. L. Harwell, and M. J. Loos, "Impact of aggressive drive cycles on motor vehicle exhaust pm emissions," *Journal of Aerosol Science*, vol. 113, pp. 1–11, 2017.

[23] P. Kalaivani and C. S. Joice, "Design and modelling of a neural network-based energy management system for solar PV, fuel cell, battery and ultracapacitor-based hybrid electric vehicle," *Electrical Engineering*, vol. 106, no. 1, pp. 689–709, 2024.

[24] Y. Al-Wreikat and J. R. Sodre, "Evaluating the energy consumption of an electric vehicle under real-world driving conditions," *SAE International Journal of Advances and Current Practices in Mobility*, vol. 5, no. 2022-01-1127, pp. 1256–1263, 2022.

[25] R. Arun Chendhuran and J. Senthil Kumar, "Review of model-based state-of-charge estimation methods for batteries of electric vehicles," in *International*

Conference on Automation, Signal Processing, Instrumentation and Control, pp. 2619–2625, Springer, 2020.

[26] E. Chemali, P. J. Kollmeyer, M. Preindl, and A. Emadi, "State-of-charge estimation of li-ion batteries using deep neural networks: A machine learning approach," *Journal of Power Sources*, vol. 400, pp. 242–255, 2018.

[27] E. Chemali, P. J. Kollmeyer, M. Preindl, R. Ahmed, and A. Emadi, "Long short-term memory networks for accurate state-of-charge estimation of li-ion batteries," *IEEE Transactions on Industrial Electronics*, vol. 65, no. 8, pp. 6730–6739, 2017.

[28] Y. LeCun, Y. Bengio, and G. Hinton, "Deep learning," *Nature*, vol. 521, no. 7553, pp. 436–444, 2015.

[29] S. Lathuilière, P. Mesejo, X. Alameda-Pineda, and R. Horaud, "A comprehensive analysis of deep regression," *IEEE Transactions on Pattern Analysis and Machine Intelligence*, vol. 42, no. 9, pp. 2065–2081, 2019.

[30] D. Zhu, J. J. Campbell, and G. Cho, "Battery voltage prediction using neural networks," in *2021 IEEE Transportation Electrification Conference & Expo (ITEC)*, pp. 807–812, IEEE, 2021.

[31] C.-W. Hsu, R. Xiong, N.-Y. Chen, J. Li, and N.-T. Tsou, "Deep neural network battery life and voltage prediction by using data of one cycle only," *Applied Energy*, vol. 306, p. 118134, 2022.

[32] A. Bhattacharjee, A. Verma, S. Mishra, and T. K. Saha, "Estimating state of charge for xEV batteries using 1D convolutional neural networks and transfer learning," *IEEE Transactions on Vehicular Technology*, vol. 70, no. 4, pp. 3123–3135, 2021.

[33] M. Naguib, P. Kollmeyer, C. Vidal, and A. Emadi, "Accurate surface temperature estimation of lithium-ion batteries using feedforward and recurrent artificial neural networks," in *2021 IEEE Transportation Electrification Conference & Expo (ITEC)*, pp. 52–57, IEEE, 2021.

[34] F. Yang, S. Zhang, W. Li, and Q. Miao, "State-of-charge estimation of lithium-ion batteries using LSTM and UKF," *Energy*, vol. 201, p. 117664, 2020.

[35] J. Gaudart, B. Giusiano, and L. Huiart, "Comparison of the performance of multi-layer perceptron and linear regression for epidemiological data," *Computational Statistics & Data Analysis*, vol. 44, no. 4, pp. 547–570, 2004.

[36] P. Pillai, S. Sundaresan, P. Kumar, K. R. Pattipati, and B. Balasingam, "Open-circuit voltage models for battery management systems: A review," *Energies*, vol. 15, no. 18, p. 6803, 2022.

[37] C. Vidal, O. Gross, R. Gu, P. Kollmeyer, and A. Emadi, "xEV li-ion battery low-temperature effects," *IEEE Transactions on Vehicular Technology*, vol. 68, no. 5, pp. 4560–4572, 2019.

[38] J. He, L. Li, J. Xu, and C. Zheng, "ReLU deep neural networks and linear finite elements," *arXiv preprint arXiv:1807.03973*, 2018.

[39] S. Bock, J. Goppold, and M. Weiß, "An improvement of the convergence proof of the adam-optimizer," *arXiv preprint arXiv:1804.10587*, 2018.

[40] A. T. Hamada and M. F. Orhan, "An overview of regenerative braking systems," *Journal of Energy Storage*, vol. 52, p. 105033, 2022.

[41] A. J. Bard, G. Inzelt, and F. Scholz, *Electrochemical dictionary.* Springer, 2012.

[42] J. Grau-Moya, T. Genewein, M. Hutter, L. Orseau, G. Delétang, E. Catt, A. Ruoss, L. K. Wenliang, C. Mattern, M. Aitchison, *et al.*, "Learning universal predictors," *arXiv preprint arXiv:2401.14953*, 2024.

[43] S. B. Sarmah, P. Kalita, A. Garg, X.-d. Niu, X.-W. Zhang, X. Peng, and D. Bhattacharjee, "A review of state of health estimation of energy storage systems: Challenges and possible solutions for futuristic applications of li-ion battery packs in electric vehicles," *Journal of Electrochemical Energy Conversion and Storage*, vol. 16, no. 4, p. 040801, 2019.

[44] S.-C. Huang, K.-H. Tseng, J.-W. Liang, C.-L. Chang, and M. G. Pecht, "An online SOC and SOH estimation model for lithium-ion batteries," *Energies*, vol. 10, no. 4, p. 512, 2017.

[45] J.-F. Toubeau, B. Bakhshideh Zad, M. Hupez, Z. De Grève, and F. Vallée, "Deep reinforcement learning-based voltage control to deal with model uncertainties in distribution networks," *Energies*, vol. 13, no. 15, p. 3928, 2020.